robotics

MDPI

Article

Design and Experimental Evaluation of Multiple 3D-Printed Reduction Gearboxes for Wearable Exoskeletons

Riccardo Bezzini [1,2], Giulia Bassani [1,2], Carlo Alberto Avizzano [1,2], and Alessandro Filippeschi [1,2]*

[1] Institute of Mechanical Intelligence, Scuola Superiore Sant'Anna, 56127 Pisa, Italy; riccardo.bezzini@santannapisa.it (R.B.); g.bassani@santannapisa.it (G.B.); c.avizzano@santannapisa.it (C.A.A.)
[2] Department of Excellence in Robotics and AI, Scuola Superiore Sant'Anna, 56127 Pisa, Italy
* Correspondence: alessandro.filippeschi@santannapisa.it

Abstract: The recent advancements in wearable exoskeletons have highlighted their effectiveness in assisting humans for both rehabilitation and augmentation purposes. These devices interact with the user; therefore, their actuators and power transmission mechanisms are crucial for enhancing physical human–robot interaction (pHRI). The advanced progression of 3D printing technology as a valuable method for creating lightweight and efficient gearboxes enables the exploration of multiple reducer designs. However, to the authors' knowledge, only sporadic implementations with relatively low reduction ratios have been reported, and the respective experimental validations usually vary, preventing a comprehensive evaluation of different design and implementation choices. In this paper, we design, develop, and examine experimentally multiple 3D-printed gearboxes conceived for wearable assistive devices. Two relevant transmission ratios (1:30 and 1:80) and multiple designs, which include single- and double-stage compact cam cycloidal drives, compound planetary gearboxes, and cycloidal and planetary architectures, are compared to assess the worth of 3D-printed reducers in human–robot interaction applications. The resulting prototypes were examined by evaluating their weight, cost, backdrivability, friction, regularity of the reduction ratio, gear play, and stiffness. The results show that the developed gearboxes represent valuable alternatives for actuating wearable exoskeletons in multiple applications.

Keywords: wearable exoskeletons actuator; pHRI; 3D-printed reducers; cycloidal reducer; planetary gearbox

check for updates

Citation: Bezzini, R.; Bassani, G.; Avizzano, C.A.; Filippeschi, A. Design and Experimental Evaluation of Multiple 3D-Printed Reduction Gearboxes for Wearable Exoskeletons. *Robotics* **2024**, *13*, 168. https://doi.org/10.3390/robotics13110168

Academic Editor: Claudio Loconsole

Received: 24 October 2024
Revised: 13 November 2024
Accepted: 16 November 2024
Published: 19 November 2024

Copyright: © 2024 by the authors. Licensee MDPI, Basel, Switzerland. This article is an open access article distributed under the terms and conditions of the Creative Commons Attribution (CC BY) license (https://creativecommons.org/licenses/by/4.0/).

1. Introduction

In recent years, the development of wearable exoskeletons has seen significant growth, driven by their potential in a wide range of applications. Indeed, these devices can be used for assistance [1], rehabilitation [2], and augmentation [3]. Several research efforts aimed at enhancing wearable exoskeletons focus on mechanical [4] and control [5] solutions to improve performance in terms of physical human–robot interaction (pHRI), leading to increasingly safe and ergonomic devices that ensure efficient modulation of interaction forces tailored to specific applications.

High-performance actuators, comprising motors and power transmission mechanisms, are crucial for enhancing pHRI [6,7]. Therefore, the actuation modules of exoskeletons must be efficient while ensuring low costs and weights to maintain the affordability and usability of the device [8]. Among the diverse methods for actuating wearable exoskeletons, electric motors with high torque density, paired with suitable gearing systems, stand out as valuable and common solutions [9]. The literature contains multiple implementations of geared electric-motor-driven exoskeletons, such as Refs. [10–13], exhibiting a wide range of reducer designs and transmission ratios tailored to the specific requirements of different applications.

Despite the undeniable value of current 'geared' exoskeletons, the use of transmission mechanisms introduces challenges such as increased complexity, weight, and cost. Since

reducing weight and cost is desirable for exoskeletons, some studies have explored using 3D-printed components to develop lighter wearable robots [14,15]. However, given the recent advancements in additive manufacturing (AM), 3D-printed components also emerge as a promising option for developing efficient, lightweight, and cost-effective reducers, and are also capable of enhancing pHRI in robotic exoskeletons, thus addressing the issues of rising costs and weights associated with traditional reduction gearboxes.

Several studies have assessed the value of using polymeric materials for building gears. For example, Ref. [16] investigated materials for lightweight reduction gears aimed at reducing robot weight by using composite materials and resins. Weight reduction tends to decrease stiffness, resulting in a drop in speed and precision performance. The authors evaluated the applicability of replacing metal parts with plastic materials produced by a fused deposition modeling 3D printer. In other works, such as Refs. [17–19], the authors evaluated the influences of multiple printing parameters such as the printing nozzle temperature, speed, printing bed temperature, and infill percentage, while assessing fatigue life and the failure types of 3D-printed gears made of polylactic acid (PLA). In [20], the authors carried out experimental determinations to generate new insights regarding the capability of 3D-printed gears to function in mechanisms without lubrication, considering factors like sliding speed, material hardness, surface finish, and geometry. Moreover, some studies focused on evaluating dimensional accuracy, form errors, and surface quality regarding FFF (fused filament fabrication) [21,22].

However, to the authors' knowledge, only a few recent studies explored the possibility of exploiting 3D-printed-geared transmission in wearable devices [23–25]. Other works presented scattered implementations with isolated experimental investigations of 3D-printed reducers, which do not allow for comparisons between different gearbox designs and reduction ratios. For example, in [26,27], the authors presented 3D-printed actuators, but they limited the study to low reduction ratios (from 1:7.5 to 1:15), only considering the classic planetary design and its compound variation. Other studies focused on 3D-printed cycloidal reducers, such as Refs. [23,28,29], where the authors presented design details and experimental results, focusing on single low-ratio (1:11 and 1:30) cycloidal reducers.

Notwithstanding the merits of the mentioned works, the literature lacks a more extensive and comprehensive evaluation of 3D-printed reducers. Therefore, the goal of this work is to investigate and compare multiple 3D-printed reducers to examine the possibility of using such mechanisms in wearable exoskeletons and enhance proper pHRI.

This study presents a fairly wide-ranging comparison of 3D-printed reducers, exposing lightweight and low-cost implementations of three different transmission solutions, i.e., single- and double-stage cycloidal reducers, planetary compound transmissions, and the combination of cycloidal and planetary gearboxes in a double-stage reducer. These designs are examined by inspecting the respective performances of two reduction ratios, i.e., 1:30 and 1:80, which are plausible for rehabilitative devices, as well as for exoskeletons conceived for assistance and augmentation. Overall, eight reducers are compared. Their 3D models (STL files) are available upon request to the authors, together with the list of off-the-shelf components (bearings, screws, and nuts) exploited for the assembly.

In summary, the main contributions of this paper are as follows:

- The design and realization of eight different 3D-printed reduction gearboxes, for a comprehensive evaluation of their features.
- A comparison of multiple transmission designs and reduction ratios, which, to the authors' knowledge, have not been previously examined in the field of 3D-printed actuators (e.g., compact double-stage cycloidal reducers, high transmission ratios above 1:50, and combinations of cycloidal and planetary gearboxes).
- An experimental evaluation of multiple performance indexes (e.g., backdrive torque, friction, gear play, stiffness, etc.) for each reducer that concurrently allows for a comprehensive assessment of several transmission designs implementing different reduction ratios.

The remainder of this paper is organized as follows:Section 2 presents a brief presentation of the reduction designs exploited in this work; Section 3 presents a brief presentation of the reduction designs exploited in this work, followed by more detailed descriptions of the presented 3D-printed mechanisms. Section 4 presents the experimental setup, metrics, and test procedures. Section 5 presents some evaluative considerations on the results of the experimental analysis, discusses the different features of the investigated reduction mechanisms, focuses on the current limitations of the proposed approach, and presents the expected future works. Finally, Section 6 presents a summary of the proposed work, along with the most relevant inferences.

2. Background

2.1. Transmissions Architectures

2.1.1. Single-Stage Cycloidal Reducer

The working principle of the cycloidal reducers involves four main components: an eccentric shaft that serves as the input motion, a cycloid disk mounted on the eccentric shaft that engages with the pins (or rollers) forming the fixed cycloidal base, and a set of output pins fixed to the carrier, representing the transmission's output. The reduction mechanisms are named after the profile of the disk, which is indeed derived from a *cycloid* [30]. A simplified illustration is reported in Figure 1.

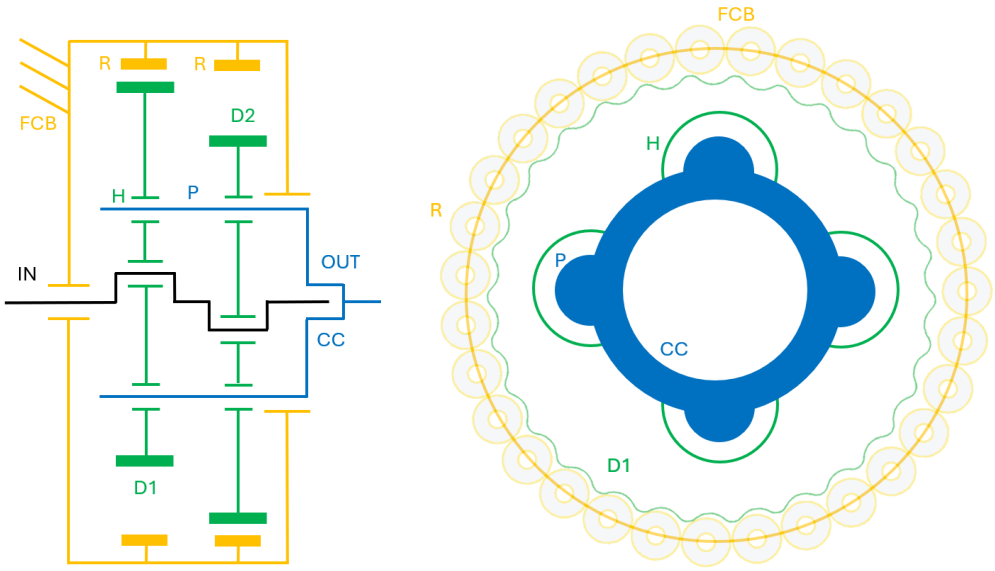

Figure 1. Schematic illustrations of the structure of the single-stage cycloidal reducer. Both the lateral (**a**) and frontal (**b**) views are reported for clarity. The acronyms used represent parts that are the same color. **IN** refers to the input shaft (in black) with eccentric sections. **FCB** refers to the fixed cycloidal base (in yellow), to which the rollers (**R**, still in yellow) are connected. **D1** and **D2** are the two cycloidal disks, in green. **CC** refers to the cycloidal carrier (in blue), which is composed of a certain number of pins (**P**) that are driven by interacting with the holes (**H**). The carrier represents the output of this reducer.

The rotation of the eccentric shaft causes the roto-translation of the cycloid disk, which engages with the cycloid base's rollers (in this case, bearings). The rotation of the disk generates the movement of the output pins in the holes in the cycloid disc. This bore–pin coupling allows the output shaft to rotate non-eccentrically. The output shaft's rotational speed can be deduced by the gear ratio, as follows:

$$i = \frac{n_l}{n_l - N_p}, \tag{1}$$

where n_l denotes the number of lobes of the cycloidal disk and N_p denotes the number of rollers connected to the fixed cycloidal base. The cycloidal base can be composed of pins or rollers (usually bearings or bushings); the main differences between these two architectures are studied in [29]. Two cycloid disks were used (each engaging with a different set of rollers), with a difference in phase of 180°, ensuring that the unbalanced forces compensate each other, resulting in smoother operation at high speeds and reduced vibrations. The two sets of rollers that engage with the disks are identical.

The cycloidal systems allow us to obtain high reduction ratios simply with a difference of only one tooth between the number of rollers and the number of lobes on the disk. These reducers also ensure lower frictions and smoother contact forces, with respect to the classic geared wheels, between the disk and the cycloidal base, composed of bearings as rollers (a *pin-wheel configuration*), allowing for more efficient contact dynamics between the disk and base (creeping contacts are prevented).

2.1.2. Double-Stage Cycloidal Reducer

As can be deduced from the previous explanation of the cycloidal reducer's architecture (especially considering Figure 1b), for high reduction ratios, the cycloidal architecture demands a high number of rollers. These rollers must be distributed along a sufficiently large circumference, which increases the reducer's width. To avoid this issue, the design proposed in [31] can be used. This architecture is illustrated in Figure 2a.

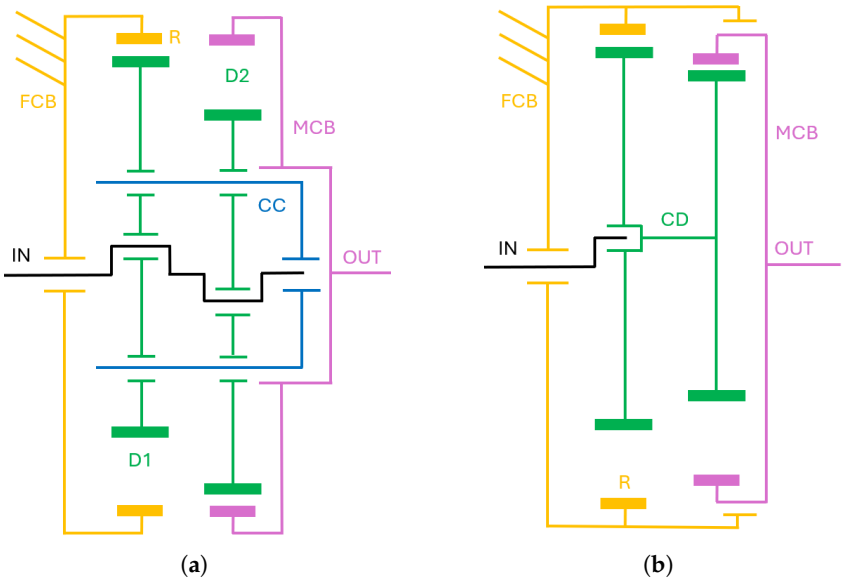

Figure 2. Schematic illustrations of the structure of the double-stage cycloidal reducer. On the left, the dual-stage double-disk architecture is presented (**a**), while on the right side, a scheme of the compact disk double-stage cycloidal reducer (**b**) is presented. The acronyms used represent parts that are the same color. **IN** refers to the input shaft (in black) with eccentric sections. **FCB** refers to the fixed cycloidal base (in yellow), to which the rollers (R, still in yellow) are connected. **D1** and **D2** are the two different cycloidal disks, which are connected to the same shaft and carrier but are in contact with two different groups of rollers. **CC** refers to the cycloidal carrier (in blue). **CD** refers to the compact disk, a part that includes two joint cycloidal disks moved by the same shaft but engaged with different sets of rollers. **MCB** refers to the moving cycloidal base, another part connected to a set of rollers (in purple), which obtains its motion from the interaction with the second disk **D2** and corresponds to the output of this reducer.

This design allows for high reduction ratios while maintaining reasonable encumbrance since the reduction ratio is computed as follows:

$$i = \frac{n_1}{N_2}, \tag{2}$$

where n_1 denotes the number of lobes of the disk of the first cycloidal stage, while N_2 denotes the number of rollers that compose the moving cycloidal base, which is the base of the second cycloidal stage.

However, this design maintains the presence of a carrier, which inevitably leads to the presence of screws (used to increase the resistance of the pins) and bearings, which are mounted in the holes of the cycloidal disks to improve the contact dynamics between output pins and disk holes.

To avoid these problems, some works (e.g., [32,33]) exploit an alternative version of a double-stage cycloidal drive, with a compact disk (composed of two joint disks) that avoids the presence of a carrier, allowing for a significant decrease in weight and cost. This architecture's reduction ratio is computed as follows:

$$i = \frac{n_1 N_2}{n_1 N_2 - n_2 N_1}, \tag{3}$$

where n_1 denotes the number of lobes of the disk of the first cycloidal stage, N_2 denotes the number of rollers that compose the moving cycloidal base (the base of the second cycloidal stage), and n_2 denotes the number of lobes of the second-stage cycloidal disk.

2.1.3. Cycloidal–Planetary (CP) Series Reducer

Planetary transmissions have four main components: the sun gear, planetary gears, the carrier, and the ring gear, which is the only internally toothed component of the reducer. This kind of mechanism comprehends several modes of operation, determined by which parts are fixed and which parts rotate. Typically, only two of the three sets of gears will rotate. Concerning the implementations presented in this work, the planetary configuration consists of a fixed ring gear, a rotating sun gear as the input, and a rotating carrier (connected to the planet gears) as the output.

The gear ratio in a planetary transmission is determined by the difference in the number of teeth on the ring gear and the sun gear. Given the following equations, which represent the sun–planet and planet–ring interactions, respectively, the overall gear ratio of a planetary gearbox can be deduced in the generic case, which involves the rotation of the gears:

$$N_s\omega_s + N_p\omega_p - (N_s + N_p)\omega_c = 0 \tag{4}$$

$$N_r\omega_r + N_p\omega_p - (N_r + N_p)\omega_c = 0 \tag{5}$$

where N stands for the number of teeth, ω represents the rotating velocity, and the subscripts s, p, r, and c denote *sun*, *planet*, *ring*, and *carrier*, respectively. Concerning the planetary gearsets presented in this work, we consider the relation between the number of teeth:

$$N_r = N_s + 2N_p. \tag{6}$$

Moreover, as mentioned previously, the ring gear is fixed in the designed gearboxes, so $omega = 0$. Finally, the transmission ratio considered here for the single-stage planetary transmissions is as follows:

$$\frac{\omega_c}{\omega_s} = \frac{N_s}{N_s + N_r}. \tag{7}$$

Usually, simple epicyclic planetary stages used with a stationary ring gear are used for implementing gear ratios that vary from 1:3 to 1:9.

The **CP** reducers are designed as a series combination of cycloidal and planetary reducers. The output of the cycloidal stage (the carrier) serves as the input for the subsequent planetary stage, the sun. This configuration optimizes the unique advantages of each type: cycloidal reducers with lower ratios provide manageable radial dimensions, and planetary

stages, as mentioned previously, are limited to reduction ratios up to 1:9 [34]. The resulting gear ratio can be deduced by combining 1 and 7, obtaining Equation (8):

$$i = i_{cycloidal}\, i_{planetary} = \frac{N_s}{N_s + N_r}\, \frac{n_l}{n_l - N_p}. \tag{8}$$

In Figure 3, a schematic representation of the cycloidal–planetary reducer is reported.

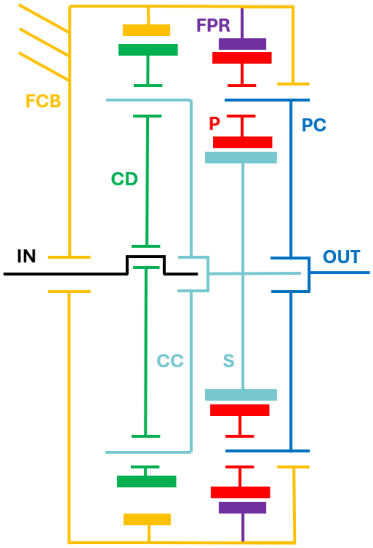

Figure 3. Schematic illustration of the structure of the cycloidal–planetary (**CP**) series reducer. The acronyms reported are abbreviations for parts of the same color. **IN** refers to the input shaft (in black) with a single eccentric section. **FCB** refers to the fixed cycloidal base (in yellow), to which the rollers (R, still in yellow) are connected. **CD** refers to the cycloidal disk. **CC** refers to the cycloidal carrier (in light blue), which is composed of another consequent section (the planetary Sun **S** joined to the first one. **P** stands for planet (in red), while **FPR** refers to the fixed planetary ring, which is rigidly connected to the cycloidal base. **PC** refers to the planetary carrier that corresponds to the output of this reducer.

2.1.4. Compound Planetary Reducer

Given the limitations of standard planetary gearboxes in achieving the high reduction ratios required for this study, the design detailed in [34] represents a suitable and compact architecture. In that work, the author analyzed and designed epicyclic gear arrangements to achieve higher gear ratios.

Due to the possibility of implementing high ratios, compound-stepped planetary gear (CSPG) drives are suitable for applications with size restrictions, e.g., gear reducers for actuators in wearable robots. The design of the reducers, shown in Figure 4 and selected from those proposed in [34], is a combination of two stages (addressed as A and B) of planetary reducers. Unlike the traditional planetary architecture, this compound transmission utilizes two ring gears: the first one (Stage A) is fixed to the stator of the motor while the second ring gear (Stage B) is the output of the reducer. The input shaft moves the sun of Stage A. Stage B does not include a sun gear. The compound planets are composed of two different base planets rigidly connected to form a single component. The reduction ratio of this reducer can be computed according to the following equation:

$$i = \frac{1 + \dfrac{z_{3a}}{z_{1a}}}{1 - \dfrac{z_{2b} z_{3a}}{z_{2a} z_{3b}}}, \tag{9}$$

where z_{ij} denotes the number of teeth of a general gear and the subscripts consist of $i \in \{1, 2, 3\}$ (these numbers denote the Sun, planet, and ring, respectively), and $j \in \{a, b\}$ (these letters denote the first and second planetary stages, respectively).

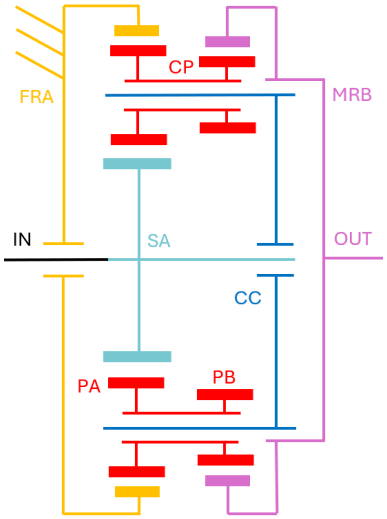

Figure 4. Schematic illustration of the structure of the planetary compound (**CO**) reducer. The acronyms used represent parts that are the same color. **IN** refers to the input shaft (in black), which corresponds to the planetary Sun **SA** of Stage A of the compound reducer. **FRA** refers to the planetary fixed ring of Stage A (in yellow). **CP** refers to the compound planet (in red), composed of two joint planets (**PA** and **PB**, respectively, the planet of Stage A and the planet of Stage B). **CC** refers to the compound carrier (in blue) to which the compound planets are connected. **MRB** refers to the planetary moving ring of Stage B, which corresponds to the output of this reducer.

3. Materials and Methods

3.1. Design Assumptions and Constraints

The first design constraint is the transmission ratio, whose selected values are 1:30 and 1:80. These values were selected because lower ratios would demand high-torque expensive motors, which is in contrast with the goal of cost-effective and wearable actuators. Instead, higher ratios may produce excessive reflected inertia and higher backdrive torques [13], which is undesirable in pHRI. To set encumbrance constraints, as references, we considered 3D-printed reducers from valuable works such as Refs. [26,28,29] (with the maximum reduction ratio of 1:15). The diameter and height constraints used in designing the target reducers were slightly reduced from the dimensions reported in previous studies. The goal was to maintain reasonable dimensions while achieving higher reduction ratios; therefore, the maximum diameter and height were set, respectively, to 100 mm and 55 mm.

3.2. Proposed Reducers

This section presents the structures of the proposed reducers. In the following, the proposed reducers will be addressed with acronyms that refer to the gearbox designs: **CY** stands for *cycloidal*, **CO** symbolizes the *compound planetary* design, and **CP** stands for the *cycloidal–planetary series*. For example, **CY30** refers to the cycloidal reducer with a ratio of 1:30, while **CO80** stands for the compound planetary gearbox with a reduction ratio equal to 1:80. Regarding the **CY80** reducers, since three versions were explored to assess the characteristics of this design, each reducer will be referred to using **CY80vx**, where $x \in \{1, 2, 3\}$.

3.2.1. CY30

For the design of this reducer and the other reducers, including the cycloidal stages, the roller choice was fundamental, since it affected the other dimensions once the reduction

ratio was set. A low roller radius allows for reduced encumbrances, but it may reduce the torque transmission capability of the reducer.

On the other hand, large rollers may lead to better torque performances. However, given the target ratio (1:30) and the constraint on the maximum diameter (100 mm), an excessively high roller diameter would not fit the design goal. Moreover, larger rollers (bearings) would cause an excessive increase in the cost and weight of the reducer. The chosen roller radius of 4 mm represents a valid compromise, balancing reducer dimensions, weight, and costs. Moreover, its internal diameter of 3 mm allows fixing the rollers to the cycloidal base using M3 screws, which is important for guaranteeing a stable and resistant connection between the base and the rollers.

Once the roller dimensions were established, the minimum possible cycloidal base radius was computed to ensure that the rollers would not interfere with each other's motion. The choice of the cycloidal base radius is also correlated with the eccentricity. Indeed, an excessively small base radius would limit the eccentricity. Given a specific roller dimension and cycloidal base radius, an increase in eccentricity could cause the cycloidal disk to have an increasingly discontinuous lateral surface, thereby resulting in severely irregular output motion. The same reasoning regarding the parameters' values was applied in the design of other cycloidal stages presented later and will not be repeated. Table 1 displays the chosen values for the design parameters of the **CY30** reducer.

Table 1. Design parameters of the CY30 reducer.

Parameter	Value
Fixed cycloidal base radius (location of rollers)	41 mm
Number of rollers	31
Roller radius	4 mm
Eccentricity	1 mm
Number of carrier output pins	6
Output pin radius	4 mm
Carrier radius	24 mm

Figure 5 represents a CAD model of the exploded view of the **CY30** reducer, without including bearings (except for the rollers) and screws. The input shaft features two opposing eccentric sections, each coupled through bearings to the disks, with one disk phased 180° opposite the other. These disks engage with two sets of rollers, separated by a row of printed spacers. Both the spacers and the rollers are connected to the cycloidal base (the lower and upper white parts) using screws and nuts. Also, screws of varying lengths are used to reinforce the pins that make up the cycloidal carrier.

3.2.2. CY80

According to the reduction ratio Formula (3), the chosen **CY80** architecture allows for multiple combinations regarding the number of rollers of the fixed and moving cycloidal bases. Apart from the number of rollers, eccentricity is the other parameter that directly influences the dimensions of the reducer.

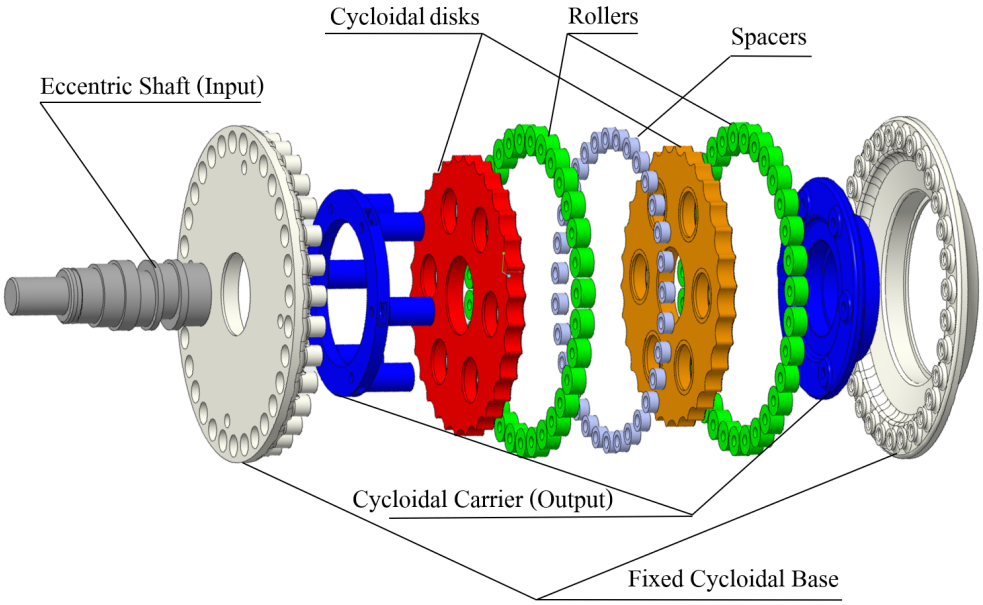

Figure 5. Exploded view of the CAD model of the cycloidal (**CY30**) reducer. Bearings, nuts, and screws were hidden for better comprehensibility of the Figure. The distinct elements illustrated with the same color (the upper and lower parts of the fixed cycloidal base, as well as the two parts of the cycloidal carrier) are rigidly connected through screws in the final assembly.

Since this reduction mechanism is not widespread (to the authors' knowledge, it was never implemented in a 3D-printed version), we designed and tested different alternatives for the number of rollers and eccentricity. This contributes to this work's goal of exploring different architectures for 3D-printed reducers. The design parameters reported in Table 2 describe the three presented design arrangements:

- **CY80v1** implements a solution with minimum dimensions. Both the number of rollers at the fixed and moving cycloidal bases are the minimum required to achieve the 1:80 ratio. Also, the eccentricity is limited to 1 mm.
- **CY80v2** implements a version with the maximum number of rollers that allows respecting the maximum diameter constraint (considering the rollers with a 4 mm radius), combined with an eccentricity that is set to 0.8 mm.
- **CY80v3** implements the reducer version with the minimum number of rollers (the same as the first version). However, the dimensions have been pushed almost to the maximum limit. Indeed, as can be noted by comparing the values from Table 2, the diameters of the cycloidal bases are the same, thus using the same number of rollers as in **CY80v1** allows for a pronounced eccentricity (2.5 mm).

Variants with both a high number of rollers and high eccentricity were avoided in order to not exceed the encumbrance constraints.

The CAD models in Figure 6 display the exploded views of the three CY80 reducers. The input shafts feature a single eccentric section, which connects to the double-stage compact disk via two ball bearings, not shown in the images. The separate stages of rollers are attached to their respective bases (either fixed or moving). The upper part of the fixed cycloidal base encloses the entire reducer and also serves as a support for the Moving Base, which is connected to it through another bearing.

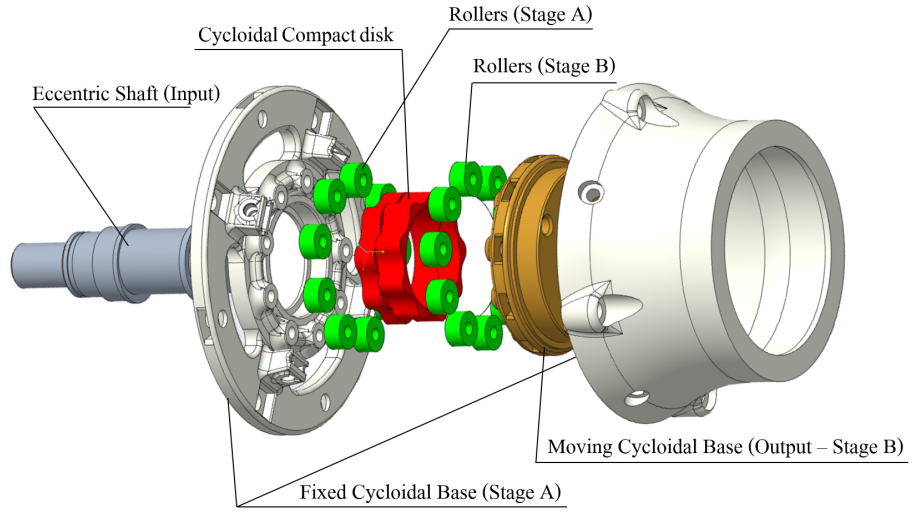

(**a**) CY80v1

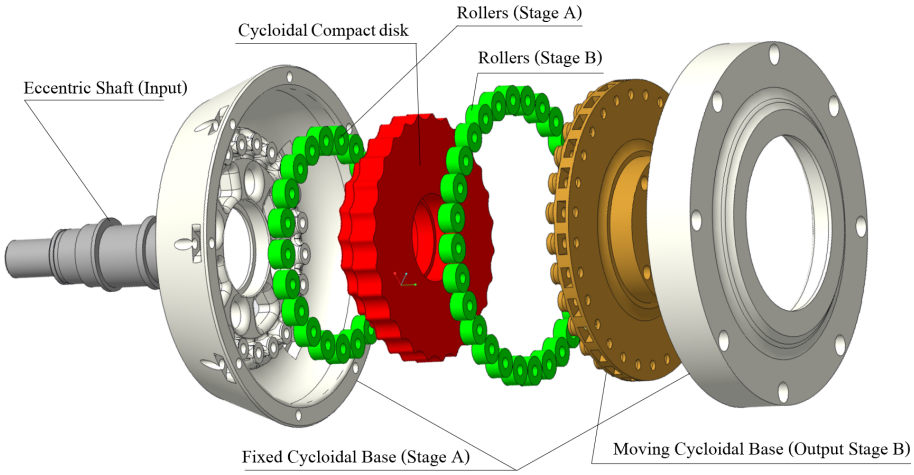

(**b**) CY80v2

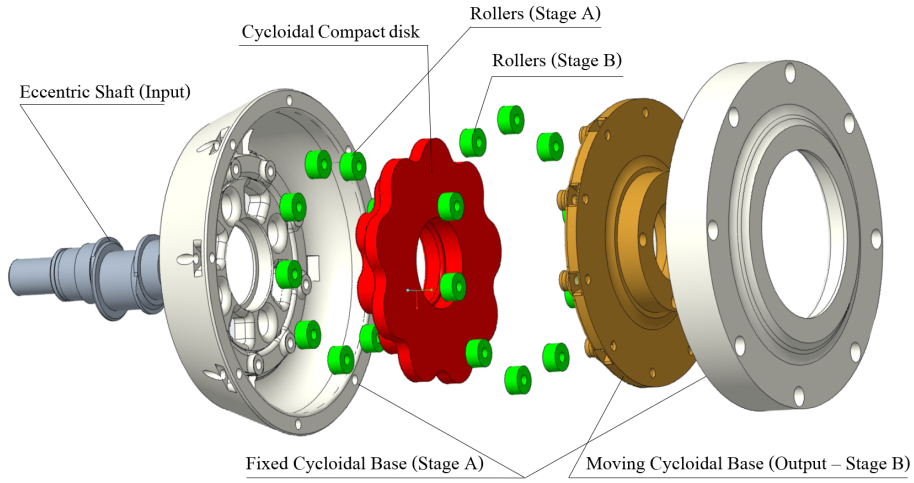

(**c**) CY80v3

Figure 6. Exploded views of the CAD models of the three cycloidal double-stage compact disk reducers (**CY80v1**, **CY80v2**, and **CY80v3**). Bearings, nuts, and screws are not shown for a better comprehensibility of the Figure. The distinct elements illustrated with the same color (the upper and lower parts of the fixed cycloidal base) are rigidly connected through screws in the final assembly.

Table 2. Design parameters of the three versions of the CY80 reducer.

Parameter	CY80v1	CY80v2	CY80v3
Fixed cycloidal base radius A (location of rollers)	18.1 mm	28.5 mm	28.5 mm
Number of rollers A	9	21	9
Moving cycloidal base radius B (location of rollers)	18.1 mm	37 mm	37 mm
Number of rollers B	10	28	10
Roller radius	4 mm	4 mm	4 mm
Eccentricity	1 mm	0.8 mm	2.5 mm

3.2.3. CP30 and CP80

For the design of the cycloidal-planetary reducers, the series combination of these architectures has necessitated joint considerations regarding dimensional compatibility for proper integration. First of all, the respective reduction ratios to be combined were selected to maximize the efficiency of the two architectures.

Since classical single-stage planetary reducers are used to implement low transmission ratios [35], we opted for 1:3 and 1:4 ratios for the total targets of 1:30 and 1:80, respectively. This led to the selection of 1:10 and 1:20 transmission ratios for the respective cycloidal stages. Since these values are lower than the 1:30 presented earlier, this design approach reduces radial encumbrances in both the **CP** reducers with respect to the **CY30**.

However, it is clear from the basic structure of a cycloidal reducer that the presence of the carrier sets an inferior limit to the reducer's diameter. A valid compromise was found with a 35 mm fixed cycloidal base radius and a 21 mm carrier radius. As noted in Table 3, these values were utilized for both the **CP** reducers as well as other design parameters.

Table 3. Design parameters of the CP30 and CP80 reducers.

Parameter	CP30	CP80
Fixed cycloidal base radius (roller location)	35 mm	35 mm
Number of rollers	11	21
Roller radius	4 mm	4 mm
Eccentricity	1.2 mm	1.2 mm
Number of cycloidal carrier output pins	6	6
Output pin radius	3.8 mm	3.8 mm
Cycloidal carrier radius	21 mm	21 mm
Number of teeth (Ring)	52	51
Number of teeth (Planets)	13	17
Number of teeth (Sun)	26	17
Number of planets	6	4
Teeth Module	1 mm	1 mm
Teeth Pressure angle	25°	25°
Planetary Carrier Radius	19.5 mm	17 mm

Once the dimensions of the cycloidal stage were set, we designed the planetary stages to keep their encumbrance smaller than the cycloidal one. The number of teeth of the external ring (together with the teeth module) determines the maximum diameter of the planetary stage. We used gears with a module of 1 mm, a practical compromise between excessively small teeth, which resulted in modest resistance and difficulties in accurately printing the gear profile, and larger modules that led to unacceptable encumbrance. The

equations below detail the relationships between the teeth module, radial encumbrance, and teeth height.

$$H_t = 2.25\,\mathrm{m}, \tag{10}$$

$$P_g = Z_g\,\mathrm{m}, \tag{11}$$

where H_t represents the height of the teeth (function of the module m) and P_g denotes the primitive circumference of the gear, which gives an approximate idea of the gear's encumbrance, and which is computed as the product of the module and the number of teeth Z_g. Once the correct ring's teeth number was set, the rest of the parameters can be deduced from Equation (7). Table 3 presents the whole set of parameters for the CP30 and CP80 reducers. The CAD models reported in Figure 7 present the exploded views of the **CP** reducers.

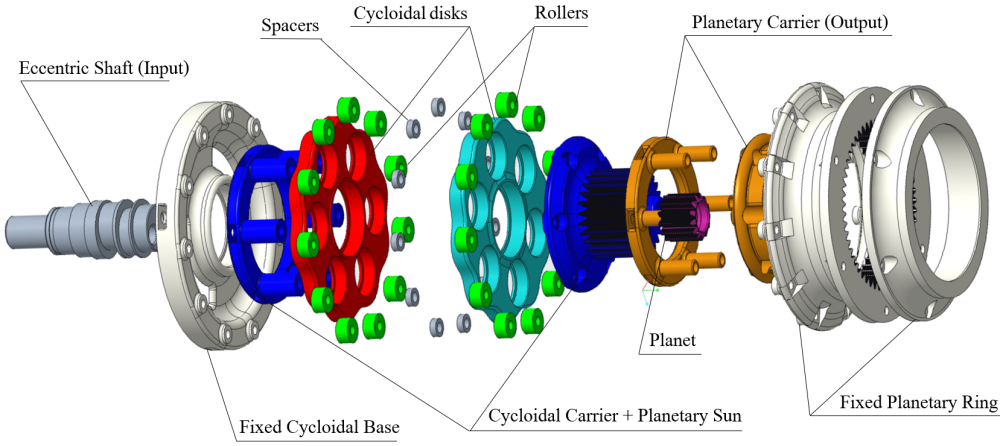

(**a**) CP30

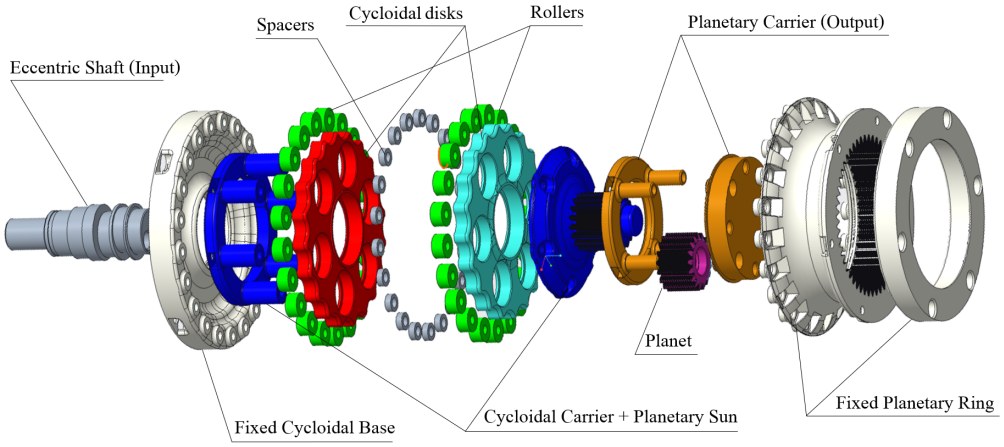

(**b**) CP80

Figure 7. Exploded views of the CAD models of both the cycloidal–planetary reducers (**CP30** and **CP80**). Bearings, nuts, and screws are not shown for a better comprehensibility of the Figure. For the same reason, not the planets are represented. The distinct elements illustrated with the same color (the fixed cycloidal base with the fixed planetary ring, the two parts of the cycloidal carrier, and the two parts of the planetary carrier) are rigidly connected through screws in the final assembly.

3.2.4. CO30 and CO80

From Equation (9), a target reduction ratio can be achieved with multiple combinations of teeth numbers. At the same time, compound reducers are not subject to the encumbrance constraints of the cycloidal stage that limited our target dimensions in the CP reducers. Therefore, we were able to increase the module to 1.2 mm, up from 1 mm in CP reducers.

The increase in the teeth module leaves room for the selection of teeth numbers, and we set the minimum number of teeth for the gears (both sun and planets) of the two stages at 16, to enable the design of carrier pins with a sufficiently large diameter. This size is crucial to accommodate two bearings for each planet for proper assembly on the carrier pin. Given these conditions, we managed to implement the minimum teeth choices that met the mentioned constraints for both **CO30** and **CO80**. As can be noticed from Table 4, the two designs presented have an equal carrier radius and almost identical dimensions.

The CAD models reported in Figure 8 present the exploded views of the **CO** reducers. The sun of the first stage (i.e., the input) engages with the Stage A planets inside the Stage A fixed ring. Given that the compound planets are composed of two different gears rigidly connected, the motion of the sun induces the common carrier to rotate; thus, the Stage B planets engage with the Stage B ring, which is the output of the reducer.

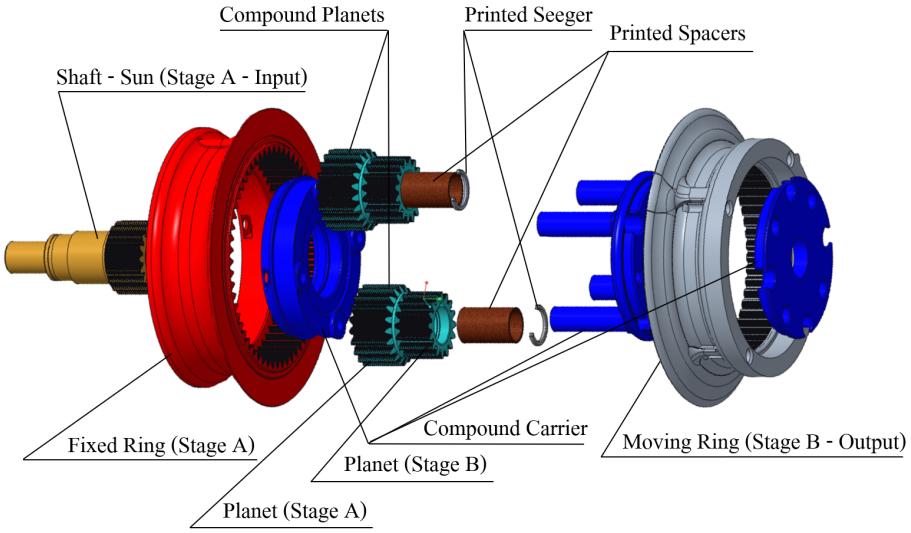

(**a**) CO30

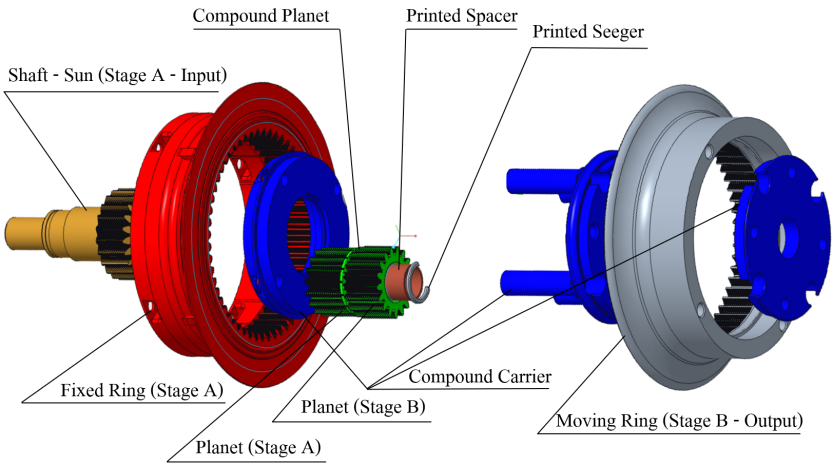

(**b**) CO80

Figure 8. Exploded view of the CAD model of both planetary compound reducers (**CO30** and **CO80**). Bearings, nuts, and screws were hidden for better comprehensibility of the figure. For the same reason, not all four planets are represented. The distinct elements illustrated with the same color (the three parts of the compound carrier) are rigidly connected through screws in the final assembly.

Table 4. Design parameters of the CO30 and CO80 reducers.

Parameter	CO30	CO80
Number of teeth Ring A	58	54
Number of teeth Planets A	20	16
Rotation angle Planets A	81°	123.75°
Number of teeth Sun A	18	22
Number of teeth Ring B	54	55
Number of teeth Planets B	16	17
Rotation angle Planets B	123.75°	111.176°
Number of planets	4	4
Teeth Module	1.2 mm	1.2 mm
Teeth Pressure angle	25°	25°
Carrier Radius	22.8 mm	22.8 mm

3.3. Materials, Printers, and Off-the-Shelf Components

To develop the presented reducers, PLA was used since it combines reasonably low costs and valuable mechanical properties [21]. The printers used were the Ultimaker S7 Pro Bundle and the Ultimaker S3-Extended, with Ultimaker Cura used as a slicer. The parts that were not produced through 3D printing were the bearings, screws, and nuts. Indeed, apart from the mentioned components, spacers and Seeger rings were produced through printing procedures.

The lists of necessary non-printed components for each reducer are presented in the tables in Appendix A. Apart from the bearings, which are clearly essentials in the reducers' structures, off-the-shelf components (especially the screws) were fundamental in strengthening some highly loaded structural components, such as the carrier pins in the exploited designs, and linking the rollers to the cycloidal bases.

3.4. Evaluation Metrics

To evaluate the features of the proposed reducers and compare different reduction ratios implemented through multiple designs, the following metrics were taken into consideration when designing the experimental protocols described in the next section:

Speed regularity: This parameter describes the oscillating deviation between the actual output speed of a reducer (given a specific motor speed) and its expected value. It is calculated as the product of the motor's speed and the reduction ratio, according to the following formula:

$$R = 100\left(1 - \frac{\Delta\omega_r}{i\,\omega_m}\right), \tag{12}$$

where R denotes the regularity (expressed as a percentage value), ω_r denotes the reducer's speed, i denotes the transmission ratio, and ω_m denotes the motor's velocity.

It is important to evaluate the regularity of a reducer to assess the precision and stability of the actuator's ability to maintain a specific velocity

Friction: This refers to the torque that the motor must generate to overcome the static (Coulomb) and dynamic (viscous) forces that resist the reducer's motion. Understanding the actuator's internal friction is essential for implementing friction compensation, which significantly enhances transparency in pHRI.

Gear play: The range of motion of the reducer's output (in the locked-input condition) that can be observed without sensing resisting torques from the actuator. Lower gear play corresponds to a more precise motion of the actuator.

Gear stiffness: The relation between the torque applied to the output of the reducer (in the locked-input condition) and the consequent motion monitored at the output itself. This parameter has preferred values, depending on the application of the actuator itself. For example, a stiffer actuator increases precision in trajectory following control, while a more compliant system can be preferred for a smoother pHRI.

Backdrive torque: The static torque that has to be applied to the output link of the reducer to initiate the motor's motion. This feature is essential in wearable devices that should function without obstructing the user's voluntary motions.

Size, weight, and cost: Ultimaker PLA (polylactic acid) was used for the development of the reducer components, meaning that the transmission masses, encumbrances, and costs are primarily influenced by the bearings and screws used, depending on their quantities. Wearable devices should be as lightweight and compact as possible to enhance user acceptance and usability. Moreover, ensuring cost-effective actuators while maintaining valuable performance is crucial for broadening the use of assistive wearable devices in both work-related environments and everyday-life applications.

4. Experimental Assessment

This section first describes two configurations of the experimental setup used to identify the investigated features. Then, the experimental procedures for each test are presented.

4.1. Experimental Setup

Figure 9 presents the setup with photos and CAD models of the two possible experimental arrangements, addressed as **C1** and **C2**, reported, respectively, in Figure 9a,b. Figure 9c highlights the main hardware components.

The experimental setup is composed of the brushless motor (EC 90 flat, 360 W, ϕ 90 mm, Maxon, Bad Homburg, Germany) with an integrated 2-channel encoder (MILE 512–6400 CPT, Maxon) coupled to the reducer's input through the motor support. The reducer's output is coupled to the incremental magnetic encoder (H2 Series, Phoenix America, Fort Wayne, IN, USA) through the encoder support, the output link, and the output shaft. These components are fixed to a vertical beam with a 3D-printed support structure.

The motor-encoder assembly is controlled by the three-phase brushless DC motor driver (STEVAL-SPIN3201, STMicroelectronics, Geneva, Switzerland). The magnetic encoder and the two load cells (CZL635, Phidgets Inc.), placed in a case on the output arm, are connected to the STM32 Nucleo-144 development board (NUCLEO-F767ZI, STMicroelectronics). Both boards are connected to the central unit (Intel NUC 11 Pro, i7-1165G7) running Windows 11 and Simulink (MATLAB, Mathworks Inc., Natick, MA, USA), where a PID (*discrete PID controller,* Simulink block) controls the speed, and a Kalman filter estimates the motor speed.

4.2. Experimental Protocols and Metrics Examination

The experimental apparatus allows testing the reducers and comparing their characteristics through the evaluation of their performances via multiple procedures. Before testing the reducers' performances, we identified the motor's torque constant as well as the motor's static and viscous internal friction. To identify the torque constant, we operated the motor at a constant velocity while it exerted constant torques to move known loads. We determined the motor's internal friction by driving the motor to follow multiple low-frequency speed sine references. The registered current data were used to implement the motor's friction compensation.

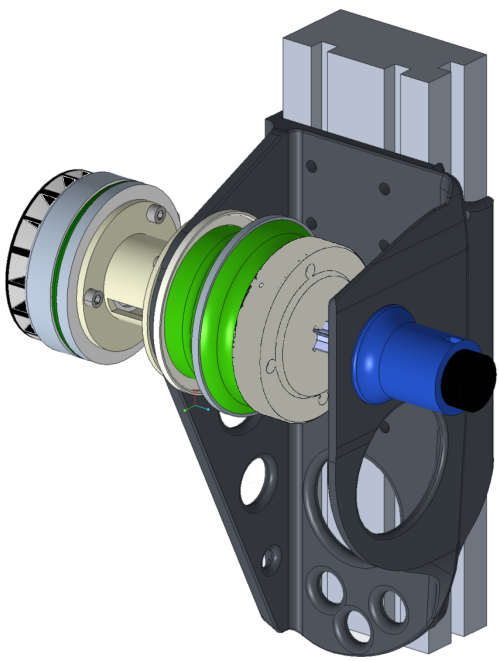

(**a**) C1 configuration.

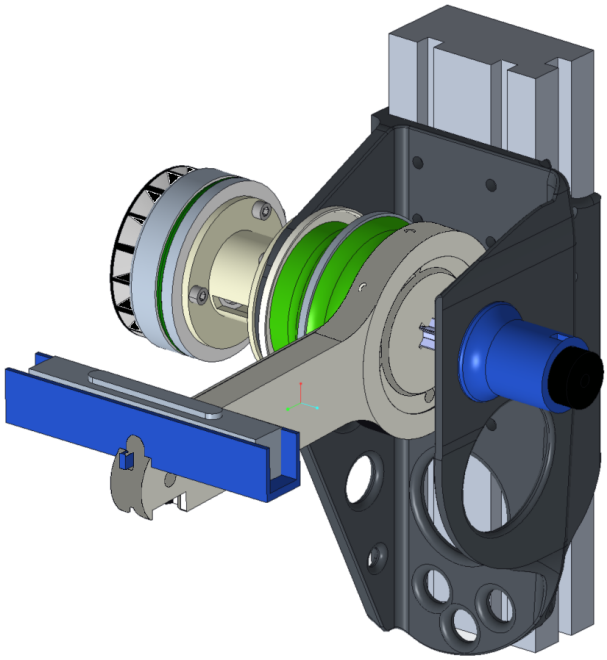

(**b**) C2 configuration.

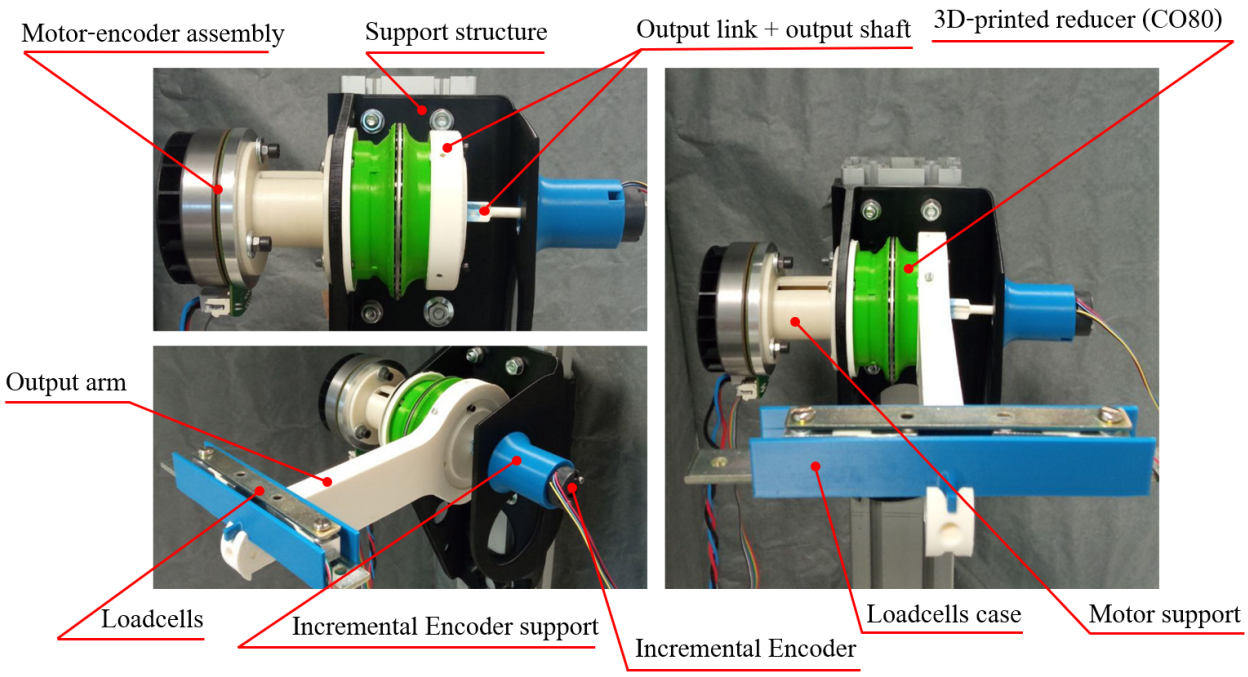

(**c**) Photos of the two experimental arrangements.

Figure 9. Experimental apparatus for testing the reducers. In Figures (**a**,**b**), the CAD models of the **C1** and **C2** arrangements of the experimental setup are presented for a clearer view. (**c**) Photos and notes to clarify the composition of the experimental setup (the reducer is the **CO80**) both in the configuration with and without the output arm and the load cells.

4.2.1. Speed Regularity

This test required using the **C1** experimental setup. To evaluate the speed regularity, the PID speed control was used to control the motor velocity, setting a sequence of step references from 20 rad/s to 120 rad/s, with 20 rad/s increments. The same test was repeated three times for each reducer with positive speed references, and three times

with negative velocities. For each speed step, the mean oscillation of the reducers' output velocity around the target value is monitored and divided by the actual target speed, as specified in Equation (12).

4.2.2. Friction

This test required the **C1** experimental setup. Transmission friction was estimated by imposing motor speed sinusoidal references in the range of ± 100 rad/s with a frequency of 0.005 Hz. The *Sine Wave* Simulink block was used to generate the reference signal. For this procedure, we followed the methodologies described in references [28,36]. Each reference signal was followed by the motor for at least three different periods, i.e., more than 6 min. The same experiment was repeated three times for each reducer, Velocity and current were registered during this procedure. Subsequently, the following friction model was fit for each reducer:

$$\tau_{fr} = \begin{cases} S_c + D_v \dot{q} & \text{if } \dot{q} \geq 0 \\ -S_c + D_v \dot{q} & \text{if } \dot{q} \leq 0 \end{cases} \tag{13}$$

where τ_{fr} denotes the friction torque, S_c denotes the static Coulomb friction component, D_v denotes the dynamic viscous factor, and $\dot{q}$ denotes the motor velocity. The current information was reported to torque data by multiplying them by the motor's current constant.

4.2.3. Gear Play

This test required the **C2** experimental setup. Gearing play was estimated by measuring the maximum possible output motion (variation in the output magnetic encoder data) without motion of the motor axis, which was detected using the motor-integrated encoder data. This experiment involved manually moving the output arm to different positions over a full output turn without applying significant torque, to prevent joint stiffness from influencing the measured output shaft motion and leading to inaccurate gear play estimates. For each reducer, these tests were conducted during three separate experimental sessions.

4.2.4. Gear Stiffness

This test required the **C2** experimental setup. Transmission stiffness was estimated by manually applying a series of loads to the load cell assembly, mounted on the arm (with a 0.2 m lever) while monitoring the current load cell force signal. This was repeated six times for each reducer, around different output positions with 60° increments, to account for position dependence. We sampled the applied torque values by multiples of 5, then we evaluated a possible linear fit that produced a valuable estimated reducer's stiffness, i.e., the torque-displacement ratio.

4.2.5. Backdrive Torque

This test required the **C2** experimental setup. To obtain information about the backdrivability of the full actuator, i.e., the motor connected to each of the reducers, we exploited the combination of arm and load cells. The motor was initially positioned to make the output arm horizontal, providing a reference for adjusting the torque due to the weight of the arm and the load cells, which varies with the analyzed angular position. Gradually increasing forces were manually applied to the load cells until the motor began to move. This procedure was repeated at least five times during each of the three different experimental sessions.

The value of the backdrive torque was estimated by detecting motor movement and evaluating the corresponding applied torque. To accurately sample the torque value required to initiate the backdrive motion, we selected an angular displacement threshold of 0.175°, which is twice the encoder resolution, to detect the onset of motor movement. The corresponding torque value was identified for each experiment.

As mentioned before, The considered torque is the sum of the forces manually applied to the load cells, as well as the weight of the 3D-printed arm and the load cells themselves. This torque is then adjusted based on the output angle relative to the horizontal position.

4.2.6. Encumbrance, Weight, and Cost

Regarding the sizes of the reducers, their maximum height and diameter were obtained from the model and verified through the measurements. To evaluate the cost, the sum of the prices of the non-printed components (bearings, screws, and nuts) was added to the cost of the printed parts. The values of the PLA elements were estimated based on their weights by considering the price of the used material as the sum of the material cost, the amortization of the printer estimated on the printer's whole life, and the energy supply cost.

The prices of the non-printed components (reported from the webpage of the same dealer) were considered based on the quantities necessary for each reducer: for example, when buying a certain quantity of the same bearing, the cost per unit decreases. Therefore, the cost of each reducer depends on the number of units of the same components that constitute it. The weights of the reducers were simply measured through a scale.

5. Results and Discussion

The experimental data gathered through the previously mentioned procedures allowed for a fair comparison of the reducers' performances and characteristics in relation to the described metrics.

5.1. Speed Regularity

In Figure 10, one of the sequences of the speed steps performed by the motor-reducers system is represented by the reference signal and both the motor and the output velocities.

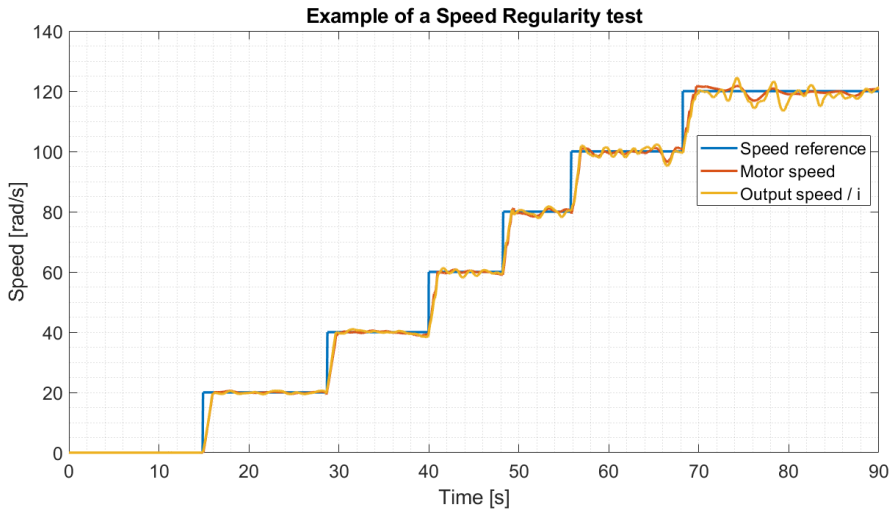

Figure 10. Representation of the data from one of the performed speed regularity tests. The reference signal (in blue) consists of a series of speed steps (from 0 rad/s to 120 rad/s, with steps of 20 rad/s). The other signals represent the motor and the reducer's output velocities (the latter was corrected through the reduction ratio, i.e., i, to plot it together with the motor's speed).

The latter was multiplied for the specific ratio to clarify the comparison with the motor velocity. It has to be noted that, for the regularity evaluations, the data from the velocity transient phases were ignored. Table 5 presents the reducers' regularity values for the evaluated velocities. The best values for each velocity step are presented in bold characters. The mean and standard deviation values for each reducer are reported in the first column of Table 6.

Table 5. Regularity of the reducers at the investigated motor velocities.

Motor Speed [rad/s]	20	40	60	80	100	120
CY30 Regularity [%]	96.05	95.29	95.65	97.37	96.4	95.9
CO30 Regularity [%]	**97.86**	96.55	**95.88**	**96.75**	**97.09**	**96.41**
CP30 Regularity [%]	95.5	94.8	95.77	95.85	94.87	96.25
CP80 Regularity [%]	95.9	**96.88**	94.9	94.35	95.51	95.68
CO80 Regularity [%]	94.4	94.89	95.33	96.51	95.07	95.84
CY80v1 Regularity [%]	91.29	92.3	92.73	92.12	93.87	93.43
CY80v2 Regularity [%]	93.85	93.1	95.69	95.97	94.55	95.28
CY80v3 Regularity [%]	88.58	89.41	90.82	89.32	88.87	90.36

Table 6. Table of the results from the tests carried out with the **C1** experimental setup.

ID	Regularity [%]	Static Friction [mNm]	Viscous Friction [mNms/rad]
CY30	96.11 ± 0.72	20.3 ± 0.64	$1.78 \pm 0.11 \cdot 10^{-1}$
CY80v1	93.12 ± 1.70	14.2 ± 0.42	$1.22 \pm 0.09 \cdot 10^{-1}$
CY80v2	94.76 ± 1.1	14.6 ± 0.48	$1.34 \pm 0.12 \cdot 10^{-1}$
CY80v3	89.56 ± 0.86	23.4 ± 0.65	$1.49 \pm 0.08 \cdot 10^{-1}$
CO30	$\mathbf{96.96 \pm 0.59}$	22.3 ± 0.71	$0.91 \pm 0.11 \cdot 10^{-1}$
CO80	95.34 ± 0.75	28.5 ± 0.93	$\mathbf{0.82} \pm 0.07 \cdot 10^{-1}$
CP30	95.51 ± 0.57	$\mathbf{13.4} \pm 0.39$	$1.16 \pm 0.09 \cdot 10^{-1}$
CP80	95.54 ± 0.87	13.7 ± 0.75	$1.59 \pm 0.10 \cdot 10^{-1}$

By comparing the regularity values across different monitored motor speeds, we demonstrated that regularity does not deteriorate with the evaluated speeds. Therefore, the performance of the reducers remains consistent at higher speeds, which is a beneficial feature for transmission.

From Table 5, it is clear that—for most of the considered motor speed values—the best regularity was achieved by the **CO30** reducer. Valuable performances were verified for the **CY30** reducer. Regarding the other presented gearboxes, from Table 5, it can be seen that the worst results were registered for **CY80v1** and **CY80v3**, which showed remarkably higher oscillations during the speed regularity tests. Concerning the contribution of the cycloidal profiles' parameters, the measured regularities suggest that an increment in the eccentricity leads to an increment of the speed fluctuations' amplitude. Indeed, **CY80v3** (which features the highest eccentricity among the cycloidal stages reported in this work) presents the highest oscillations for the tested velocities. The regularity difference between **CY80v1** and **CY80v2** can be attributed to the difference in the number of lobes. A higher number of rollers in both cycloidal stages ensures smoother motion of the cycloidal disk, as it maintains contact with more rollers during rotation. For a similar reason (considering the standard cycloidal gearbox used in **CY30**) we can justify the high regularity of the 1:30 cycloidal reducer. Lastly, the **CP** reducers exhibit reasonable regularities, considering both the 1:30 and 1:80 reducers. Indeed, these reducers were designed with relatively low eccentricity, which, combined with the planetary stage, resulted in acceptably regular reducers.

To summarize, the proposed **CY80** architecture exhibited the greatest velocity deviations, while **CP80** demonstrated the highest regularity among the 1:80 reducers.

It should be noted that features such as regularity are strongly influenced by the lack of reproducibility and tolerance limitations linked to the process of fused filament fabrication. These characteristics depend on multiple settings and factors, such as the printer, the slicer, and the printing environment.

5.2. Friction

During the experimental session carried out to estimate speed regularity, we recorded motor current, which was used to estimate the torque needed to move the actuator through the motor torque constant.

The sampled motor torque and speed were used to identify the adopted friction model by computing the static and viscous friction parameters of Equation (13). An example of this process is presented in Figure 11. In Figure 12, the resulting friction models for the reducers are reported. We separately present the results regarding the two different ratios (1:30 in Figure 12a and 1:80 in Figure 12b) to avoid ambiguous superimposition of the functions.

The mean and standard deviation values for both the static and viscous friction factors of the reducers are reported in Table 6. The best values are marked in bold text.

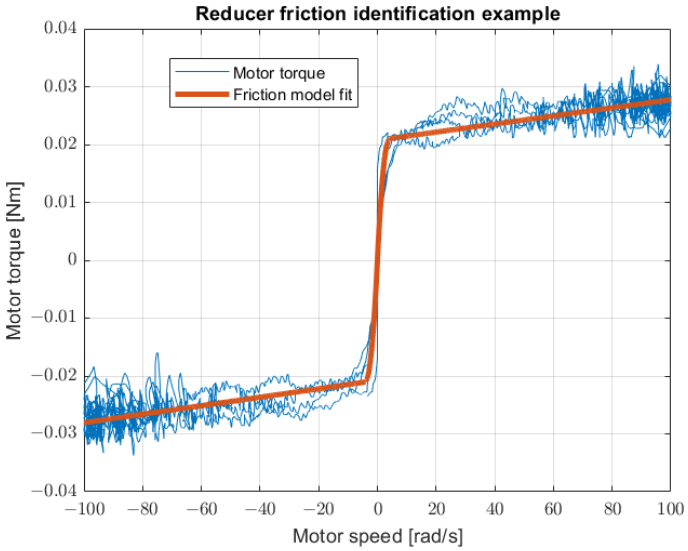

Figure 11. Example of the friction model identification of a reducer. The motor torque signal (in blue) was derived by multiplying the registered motor current by the motor's torque constant. Then, the resulting torque values were used to find the friction model's parameters and plot the fitting function (in red).

Based on the plots in Figure 12 and the values reported in Table 6, it can be noted that the architectures that incorporate a cycloidal stage (**CP** and **CY** reducers) display lower static frictions, unfortunately exhibiting higher viscous components at the same time. The opposite statements describe the **CO** models. The highest and lowest registered static friction torques are, respectively, the ones reported for the **CO80** and **CP30** reducers. Concerning the viscous component, the lowest (and, thus, the best) results were achieved by the **CO80** reducers, while the highest value is the one monitored for the **CY30**, confirming that the cycloidal reducers show higher dynamic frictions that become more prevailing with the increment of used rollers. Nonetheless, we can state that the presented reducers demonstrated valuable performances regarding their internal friction factors.

It is noteworthy that the reducers presented in this work display significantly lower frictions than the 1:11 transmissions from [28,29], regarding both the static and the viscous components, despite implementing higher reduction ratios.

Considering the potential applications of the proposed reducers in wearable exoskeletons, different requirements can be identified depending on the device's purpose. For instance, in a device where the joints frequently reverse direction, low static friction is essential. On the other hand, some applications may require high joint velocities, necessitating transmissions with low viscous friction. Based on the device's requirements, the friction model can be used to determine the torque needed by the motor to compensate for resisting forces.

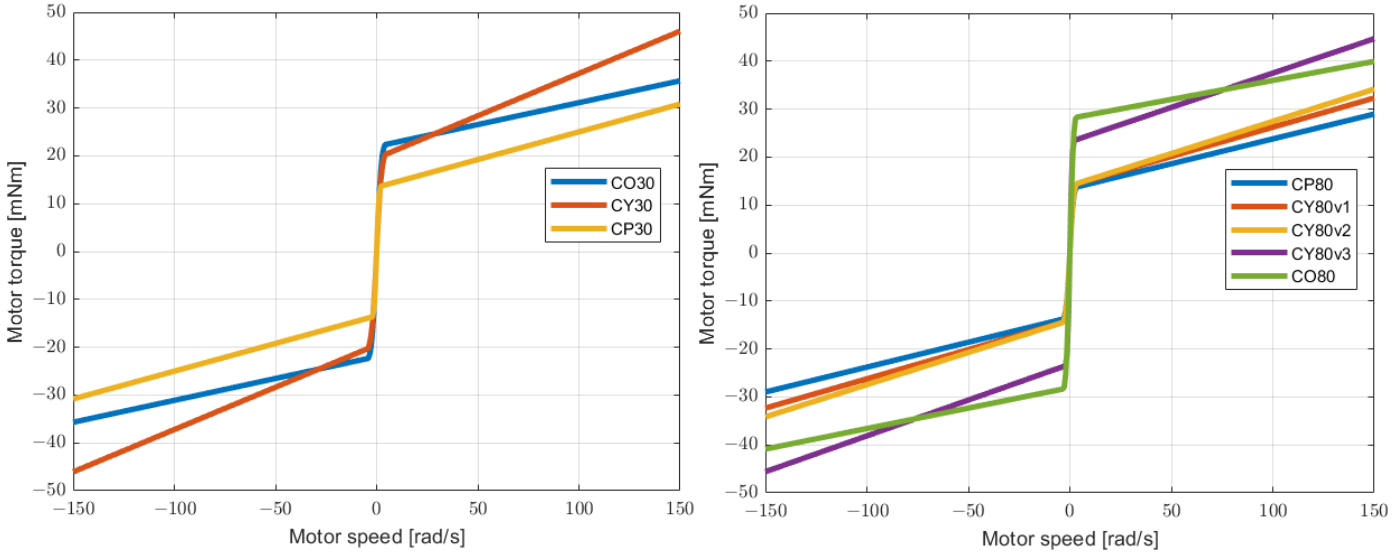

(**a**) 1:30 reducers friction models

(**b**) 1:80 reducers friction models

Figure 12. The identified friction torques for the presented reducers: (**a**) the results regarding the 1:30 reducers and (**b**) the models regarding the 1:80 reducers.

5.3. Gear Play

Gear play was estimated according to the procedure reported in Section 4.2.3. The mean and standard deviations of measured play are reported in Table 7, with the best values marked in bold text. By evaluating the gear play results reported in Table 7, the **CY** reducers display the highest range of angular motion. Concerning the **CY30** reducer, both the dimensions of the carrier pins and the surfaces of the disks affect the gear play. In the case of the **CY80** reducers, the dimensions of the disk relative to the cycloidal base rollers influence the gear play, as does the contact interface between the two components of the double compact disk.

The impact of 3D-printing constraints on dimensional tolerances, combined with repeatability issues, is particularly evident for cycloidal architectures. Indeed, the best gear play results are those presented for the **CO** reducers. Despite the underperforming CO reducers, the **CP** models display valuable gear play compared to off-the-shelf planetary gearboxes with similar transmission ratios.

Table 7. Table of the results from the tests carried out with the **C2** experimental setup.

ID	Backdrive Torque [Nm]	Gear Play [°]	Gear Stiffness [Nm/rad]
CY30	0.66 ± 0.032	1.85 ± 0.39	641.4 ± 72.73
CY80v1	>35	8.41 ± 0.58	278.1 ± 33.62
CY80v2	>35	2.69 ± 0.34	659.5 ± 52.54
CY80v3	4.89 ± 0.385	1.89 ± 0.41	344.7 ± 36.54
CO30	0.67 ± 0.040	0.53 ± 0.21	723.2 ± 71.05
CO80	>35	**0.23 ± 0.11**	821.7 ± 57.72
CP30	**0.59 ± 0.030**	1.1 ± 0.14	573.6 ± 59.52
CP80	0.70 ± 0.044	0.89 ± 0.23	472.5 ± 43.15

5.4. Gear Stiffness

The linear fitting of the motor torque-angular displacement profiles enabled the estimation of each gear stiffness. An example (for the **CO30** reducer) of the linear fit of experimen-

tal stiffness data is presented in Figure 13. The overall plot of the torque-displacement mean values for each sampled torque and linear fits for the reducers are reported in Figure 14.

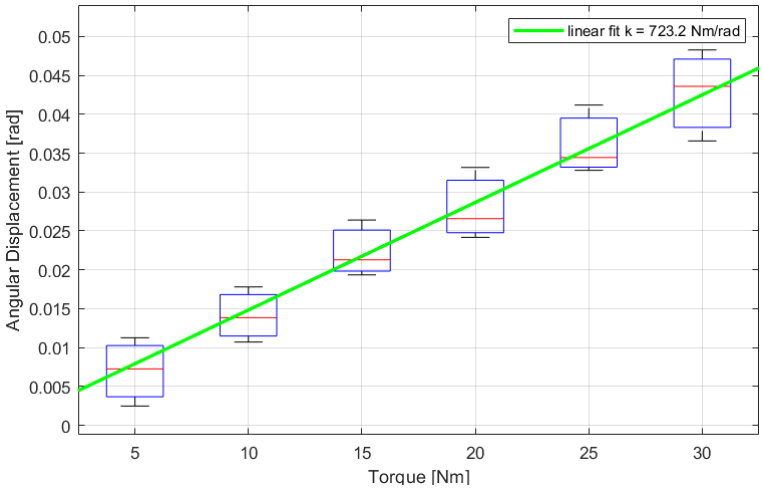

Figure 13. Instance from an experimental stiffness identification procedure. The reducer's output angular displacements are reported based on the respective torque value. Each box plot represents the distribution of the displacement data for each torque sample. The linear function describes the stiffness approximation for the **CO30** reducer.

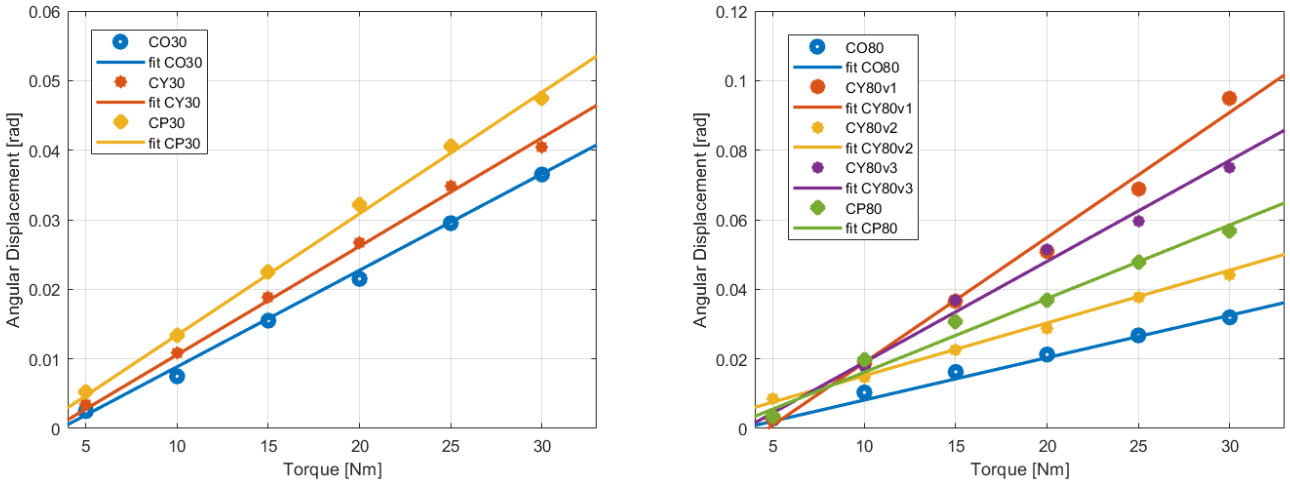

(**a**) 1:30 reducers stiffness models

(**b**) 1:80 reducers stiffness models

Figure 14. Comprehensive illustration of the linear fitted functions that approximate the reducers' stiffness based on the experimental displacement-torque data. The two reported plots present the torque-displacement mean values for each of the examined torques (displayed through different shapes and based on the reducers' architecture) and linear fit functions. Figure (**a**) presents the results regarding the 1:30 reducers and figure (**b**) reports the plot concerning the 1:80 reducers.

The stiffness mean values and standard variations are computed for each reducer by using the resulting stiffness for each of the analyzed starting positions. Considering the values reported in Table 7, the highest stiffness estimations are those related to the **CO** reducers. As mentioned before (during the evaluation of gear play, friction, and regularity) the presence of the cycloidal stage influences also the reducers' stiffness, given the nature of the contact between the rollers and the 3D-printed disks. Moreover, compared to the **CP** models, the **CO** reducers use teeth with a module of 1.2 mm, which appears to provide greater stiffness. The estimated stiffness values are 4–10 times lower than those of

commercial off-the-shelf planetary gearboxes. However, these differences are still negligible when it comes to the control of wearable exoskeletons.

Apart from the **CO** and **CP** models, the **CY30** and **CY80v2** cycloidal reducers stand out for their significant stiffness. The two remaining models, **CY80v1** and **CY80v3**, have a reduced number of rollers, resulting in limited disk-roller contact points and a smaller contact area. This feature can cause the printed disks to buckle under high torques, although it does not necessarily compromise the reducers' performances.

5.5. Backdrive Torque

The mean values and standard deviations of the computed backdrive torques (measured at the reducers' output) are reported in Table 7. The best value, that is, the one regarding the **CP30** reducers, is marked in bold text. As can be stated by the presented results, the 1:30 reducers present extremely valuable backdrive torques, such that these transmissions could be certainly used in wearable devices for assistance or augmentation.

On the contrary, **CO80**, **CY80v1**, and **CY80v2** are non-backdrivable. Thus, their uses are restricted to cases where the user's motions should not deviate from the robot's trajectory, such as in several rehabilitative devices, or in complex designs that include force sensors at the human–robot interfaces. **CY80v3** is the only CY80 model that can be backdriven. Even if the necessary torque is quite high, this result was achieved by combining the minimum number of rollers with a high eccentricity. The roller configuration used in **CY80v2** would have resulted in a backdrivable design if paired with high eccentricity, but—as discussed previously—this solution would have led to an unacceptable increase in the reducer's width.

The **CP** architecture demonstrated the lowest backdrive torque for both the 1:30 and 1:80 reducers. The **CP80** reducer stands out as the only 1:80 model that is reasonably backdrivable. Moreover, it exhibits such a low backdrive torque that it is comparable to the values obtained from the other 1:30 transmissions.

5.6. Encumbrance, Weight, and Cost

Table 8 reports the empirical data regarding encumbrances (via maximum heights and widths), weights, and costs for the presented reducers. The best values are marked in bold text. Regarding the maximum width, the best reducers are **CP30** and **CP80**. It should be noted that the **CO** reducers could have had a reduced width, but their radial encumbrance is limited by the axial bearing (as shown in the photos in Figure 15 and the CAD models 8).

Table 8. Table of the encumbrance, weight, and cost of the presented reducers.

ID	Diameter [mm]	Height [mm]	Weight [g]	Cost [€]
CY30	92	**33.5**	304	133.05
CY80v1	80	40	**184**	**51.34**
CY80v2	99	36.5	308	101.71
CY80v3	99	36.5	257	66.95
CO30	100	53.6	364	83.17
CO80	100	53.6	358	83.71
CP30	**78**	52	272	116.26
CP80	**78**	52	302	131.42

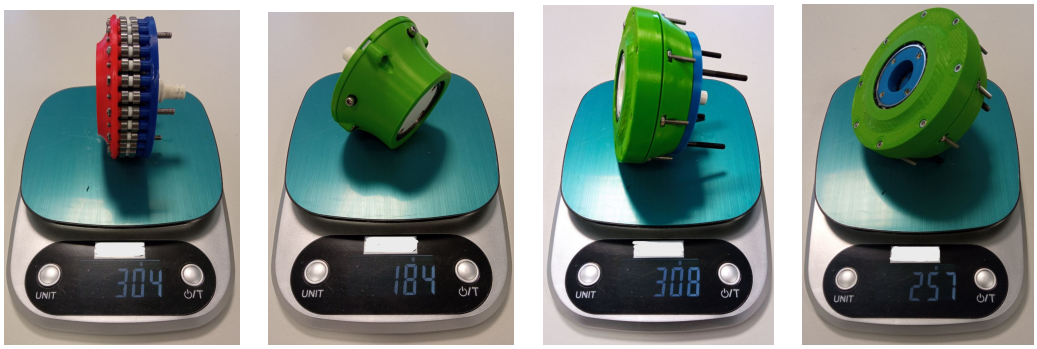

(**a**) CY30 (**b**) CY80v1 (**c**) CY80v2 (**d**) CY80v3

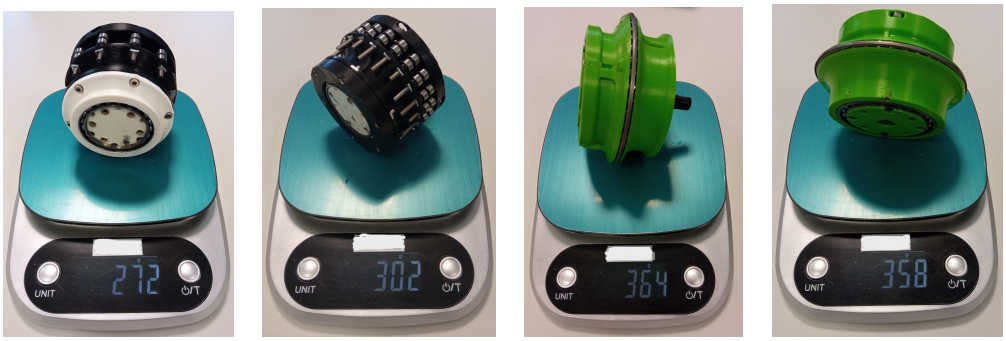

(**e**) CP30 (**f**) CP80 (**g**) CO30 (**h**) CO80

Figure 15. Photos of the designed reducers regarding the balance used to verify their weights.

Considering the reducers' heights, despite the double stage, the **CO** and **CP** reducers meet the design constraints, but the **CY** transmissions achieve the best results. In particular, **CY30** has the lowest axial encumbrance. The chosen compact disk cycloidal architecture for **CY80** guarantees optimal values since it excludes the carrier, thus reducing the reducers' height. The absence of the carrier also impacts the weight and cost of the **CY80** reducers, since without the carrier, the presence of multiple bearings, screws, and 3D-printed pins can be avoided.

The **CY30** reducer has a relatively high weight and cost, primarily due to the presence of the rollers. A similar observation applies to the **CP** reducers. However, the heaviest reducers are **CO30** and **CO80**, which—at the same time—exhibit particularly low prices, given the limited number of non-printed components.

Beyond the previous statements, which were provided to offer a clear comparison of the weights and costs of the reducers developed in this work, it is important to note that some of these transmission mechanisms have lower (or comparable) costs and weights than other 3D-printed reducers described in the literature (e.g., [27–29,37]), which nevertheless implement lower reduction ratios.

Concerning the reducers' weights, the models presented in this study display significantly lower masses with respect to the printed transmissions from other works [27–29,37], despite implementing considerably higher transmission ratios. Indeed, the mentioned works present low-reduction gearboxes (from 1:8 to 1:11), achieving masses that vary between 360 g and 780 g. The differences in the implemented reduction ratios lead to inevitable cost discrepancies. In [28,29], the authors presented cycloidal reducers with a 1:11 ratio, costing between EUR 65 and 98, resulting in more cost-effective solutions compared to some of our models. However, as discussed before, since the cycloidal architecture's cost strongly depends on the number of rollers–bearings, which increase directly with the ratio, the cost of a printed gearbox necessarily rises as the reduction ratio increases. Moreover, the lower cost achieved in [29] was realized for a reducer where the fixed outer cycloidal ring does not consist of rollers and bearings but is entirely printed, thus explaining the

significantly lower price. Nevertheless, considering the other architectures we presented, the production costs we have reported represent a noteworthy achievement given the higher transmission ratios.

Regarding the reducers' encumbrance, only the 1:10 device from [37] presented a lower diameter, while with the transmission heights, the 1:11 reducers presented in [28,29] displayed a notably lower axial encumbrance with respect to our models.

5.7. Overall Comparative Examination

In Figure 16, the spider plots of the examined features for each reducer are presented, allowing a straightforward and comprehensive assessment of the mechanisms. Different colormaps are used for each of the three main architectures presented in this work (**CY**, **CP**, **CO**). Each characteristic is displayed on a scale with maximum and minimum values specified under the metrics' names. These ranges were selected to facilitate effective visual interpretation and comparison of the reducers. The optimal value in the considered range for each feature, i.e., low backdrive torque, low cost, and low friction, is placed on the outer circumference. Consequently, the larger the area inside the spider plot, the better the performance of the reducer.

Nonetheless, it should be noted that since the ranges were specifically chosen for comparison among these reducers, a smaller area does not necessarily indicate a poor model, but rather a reducer whose performance is inferior compared to the best one obtained in this study. Indeed, the experimental results showed that each designed reducer has both benefits and drawbacks. For example, concerning the cycloidal reducers, significant differences can be observed between **CY30** and **CY80**—due to the distinct architectures used for the 1:30 and 1:80 gearboxes—and among the different implementations of the compact-double-disk design. These differences are strongly influenced by factors such as the number of rollers, the eccentricity, and the target dimensions.

Looking at Figure 16, it is clear that the **CP** architecture maintains similar attributes despite considerable differences in the transmission ratios. Indeed, the spider plots in Figure 16e,f show analogous shapes. The main differences concern the viscous friction and cost, resulting from the differing number of rollers between the two reducers.

A similar consideration can be applied to the compound reducers. In this case, however, significant differences can be found in the backdrive torque and static friction values (the **CO80** reducer was found to be non-backdrivable in our experiments).

Considering the implemented reduction ratios, the obtained weights, encumbrances, and prices turn out to be highly valuable for the developed mechanisms. Even if some of the presented models have proven themselves to be non-backdrivable, the other reducers showed significant performances regarding this feature. Concerning the identified friction components, it is clear that all proposed models exhibit considerable properties.

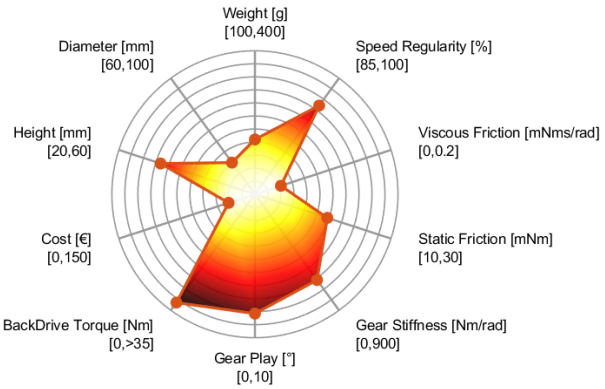

(**a**) CY30

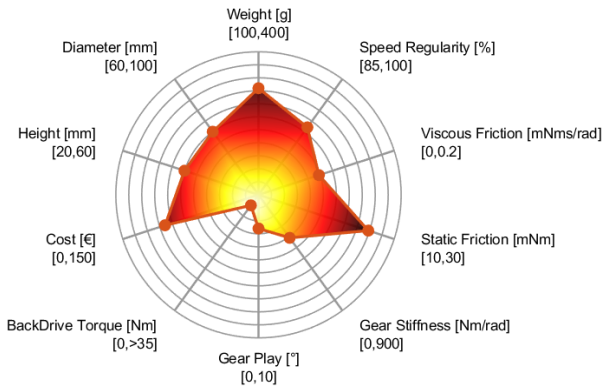

(**b**) CY80v1

Figure 16. *Cont.*

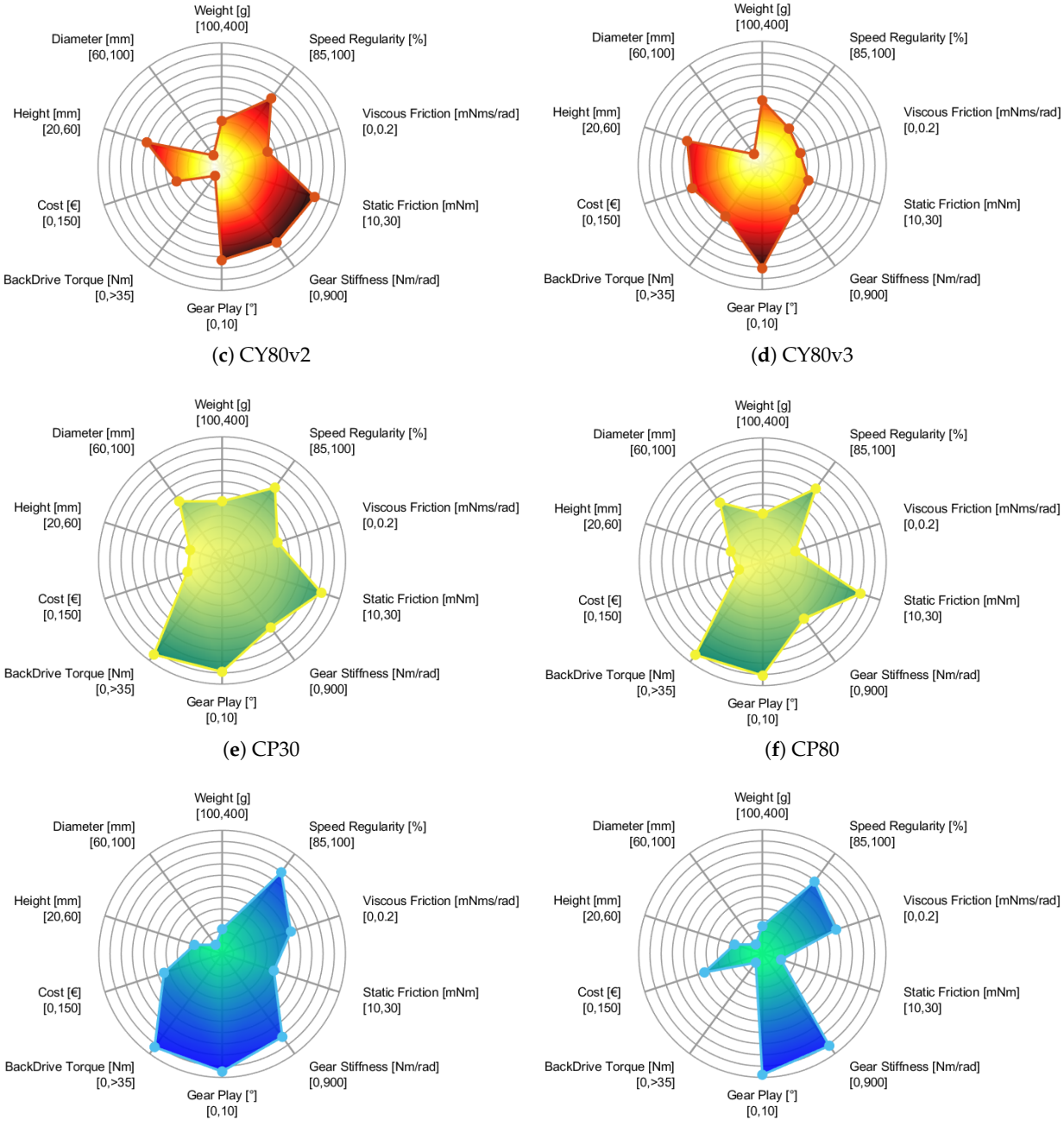

(**c**) CY80v2 (**d**) CY80v3

(**e**) CP30 (**f**) CP80

(**g**) CO30 (**h**) CO80

Figure 16. Spider plots that summarize the reducers' performances regarding the considered metrics. For each feature, the unit of measurement is specified together with the minimum and maximum values that can be reached in the plot. The best value for each metric is set on the outer circumference, which means that the larger the area inside the plot, the better the reducer. Different color maps have been adopted to distinguish different architectures.

6. Conclusions and Future Works

In this study, we designed, developed, and compared multiple 3D-printed reducers conceived for wearable assistive devices.

To provide a comprehensive evaluation of various features, we analyzed different transmission architectures. These included lightweight and low-cost implementations of single- and double-stage cycloidal reducers, planetary compound transmissions, and combinations of cycloidal and planetary gearboxes in double-stage reducers.

The general goal of our work was to investigate the prospect of using 3D-printed reducers in wearable exoskeletons, an approach that would lead to cost-effective and lightweight solutions. We examined different reducers' properties (i.e., backdrive torque, static and viscous friction, speed regularity, gear play, gear stiffness, encumbrance, weight, and cost) to inspect the different characteristics of each design and implementation and to inspect the relevance of the uses of these reducers for wearable devices. Indeed, the BOM and .stl files for reproducing the presented transmissions are available upon request from the corresponding author.

The evaluation we carried out and the subsequent considerations are meant to clarify the strengths and limitations of each reducer's 3D-printed implementation, helping to target the right architecture based on the selected task requirements. To summarize, multiple reducers showed highly valuable performances across the selected metrics, while others, notwithstanding their merits with respect to some of the analyzed features, require some improvements.

Comparing the numerical results shows that the proposed series composition of cycloidal and planetary architectures is valuable from multiple perspectives. Thus, future work will aim to perfect this design by improving its regularity while simultaneously reducing its cost and height. The planetary compound reducers mainly need enhancements in terms of encumbrance and weight. For the 1:30 cycloidal reducer, testing a smaller diameter implementation could be beneficial (also aiming to reduce costs and viscous friction). Further exploration will be carried out to model a **CY80** reducer that hopefully could combine the best features of the three implementations presented in this study.

Finally, as pointed out during the discussion of the results, the reducers evaluated in this work present significantly enhanced characteristics with respect to the mentioned state-of-the-art 3D-printed reducers, especially regarding weight, encumbrance, and friction torque.

A noteworthy limitation in our work is related to the use of the same material (PLA) for all printed components of the reducers. Clearly, different designs—such as the teeth for gears or the lobes of the cycloidal disks—could benefit from the use of various materials available for FFF. Thus, future efforts will aim to investigate the influence of different materials on the metrics considered in this work, to enhance the composition of each element in relation to its structural function. Once optimal materials are selected, we aim to optimize the design parameters to minimize encumbrance, weight, and cost of the presented reducers and improve their performance, to better suit them for use in a wearable exoskeleton.

Moreover, this work does not include an evaluation of the durability and resistance of the proposed reducers. The reason is that our primary goal and focus in this paper was to compare promising architectures for printed reducers using parameters that are typically considered when selecting a reducer for an actuator. However, structural and wear analyses represent further directions to assess and compare the proposed reducers.

Author Contributions: Conceptualization, R.B., A.F.; methodology, R.B., C.A.A. and A.F.; software, R.B., G.B., C.A.A. and A.F.; validation, R.B., G.B. and A.F.; formal analysis, R.B., A.F.; investigation, R.B.; resources, R.B., G.B., C.A.A. and A.F.; data curation, R.B.; writing—original draft preparation, R.B., G.B. and A.F.; writing—review and editing, R.B., G.B., C.A.A. and A.F.; visualization, R.B., A.F.; supervision, R.B., G.B. and A.F.; project administration, A.F.; funding acquisition, R.B., C.A.A. and A.F. All authors have read and agreed to the published version of the manuscript.

Funding: This research was funded by the Department of Excellence in Robotics and AI, Scuola Superiore Sant'Anna, 56127 Pisa, Italy.

Data Availability Statement: The data presented in this study (BOM and .stl files of the reducers' components) are available on request from the corresponding author due to privacy.

Conflicts of Interest: The authors declare no conflicts of interest.

Appendix A. Non-Printed Components

In this appendix, the non-3D-printed components used for the developed reducers are reported in the following tables.

Table A1. CY30 non-3D-printed components.

Bearings	Number of Units	Screws and Nuts	Number of Units
693	62	M3X30	2
61,700	12	M3X25	31
6802	2	M3X16	6
6803	3	M3 nuts	37
6808	1		

Table A2. CY80v1 non-3D-printed components.

Bearings	Number of Units	Screws and Nuts	Number of Units
693	19	M3X25	2
6802	3	M3X12	19
6803	1	M3X8	4
6808	1	M3 nuts	23

Table A3. CY80v2 non-3D-printed components.

Bearings	Number of Units	Screws and Nuts	Number of Units
693	49	M3X25	2
6803	4	M3X12	49
6808	1	M3X16	8
		M3 nuts	57

Table A4. CY80v3 non-3D-printed components.

Bearings	Number of Units	Screws and Nuts	Number of Units
693	19	M3X25	2
6803	4	M3X12	19
6808	1	M3X16	8
		M3 nuts	27

Table A5. CP30 non-3D-printed components.

Bearings	Number of Units	Screws and Nuts	Number of Units
693	22	M3X25	2
MR95	12	M3X20	17
61,700	13	M3X16	6
6802	3	M3 nuts	23
6808	1		

Table A6. CP80 non-3D-printed components.

Bearings	Number of Units	Screws and Nuts	Number of Units
693	42	M3X25	2
MR95	8	M3X20	27
61,700	13	M3X16	4
6802	3	M3 nuts	31
6808	1		

Table A7. CO30 non-3D-printed components.

Bearings	Number of Units	Screws and Nuts	Number of Units
MR128	8	M3X30	1
61,700	1	M4X40	4
6803	1	M4 nuts	4
6810	2		
AX 75,100	1		

Table A8. CO80 non-3D-printed components.

Bearings	Number of Units	Screws and Nuts	Number of Units
MR128	8	M3X30	1
61,700	1	M4X40	4
6803	1	M4 nuts	4
6810	2		
AX 75,100	1		

References

1. Farris, D.; Harris, D.; Rice, H.; Campbell, J.; Weare, A.; Risius, D.; Armstrong, N.; Rayson, M. A systematic literature review of evidence for the use of assistive exoskeletons in defence and security use cases. *Ergonomics* **2023**, *66*, 61–87. [CrossRef] [PubMed]
2. Zhao, C.; Liu, Z.; Zhu, L.; Wang, Y. Design and Research of Series Actuator Structure and Control System Based on Lower Limb Exoskeleton Rehabilitation Robot. *Actuators* **2024**, *13*, 20. [CrossRef]
3. Zhang, X.; Chen, X.; Huo, B.; Liu, C.; Zhu, X.; Zu, Y.; Wang, X.; Chen, X.; Sun, Q. An integrated evaluation approach of wearable lower limb exoskeletons for human performance augmentation. *Sci. Rep.* **2023**, *13*, 4251. [CrossRef] [PubMed]
4. Stroppa, F.; Soylemez, A.; Yuksel, H.; Akbas, B.; Sarac, M. Optimizing Exoskeleton Design with Evolutionary Computation: An Intensive Survey. *Robotics* **2023**, *12*, 106. [CrossRef]
5. Baud, R.; Manzoori, A.; Ijspeert, A.; Bouri, M. Review of control strategies for lower-limb exoskeletons to assist gait. *J. Neuroeng. Rehabil.* **2021**, *18*, 1–34. [CrossRef]
6. Calanca, A.; Toxiri, S.; Costanzi, D.; Sartori, E.; Vicario, R.; Poliero, T.; Di Natali, C.; Caldwell, D.; Fiorini, P.; Ortiz, J. Actuation selection for assistive exoskeletons: Matching capabilities to task requirements. *IEEE Trans. Neural Syst. Rehabil. Eng.* **2020**, *28*, 2053–2062. [CrossRef]
7. Barjuei, E.; Ardakani, M.; Caldwell, D.; Sanguineti, M.; Ortiz, J. Optimal selection of motors and transmissions in back-support exoskeleton applications. *IEEE Trans. Med. Robot. Bionics* **2020**, *2*, 320–330. [CrossRef]
8. Yu, S.; Huang, T.; Yang, X.; Jiao, C.; Yang, J.; Chen, Y.; Yi, J.; Su, H. Quasi-direct drive actuation for a lightweight hip exoskeleton with high backdrivability and high bandwidth. *IEEE/ASME Trans. Mechatron.* **2020**, *25*, 1794–1802. [CrossRef]
9. Tiboni, M.; Borboni, A.; Vérité, F.; Bregoli, C.; Amici, C. Sensors and Actuation Technologies in Exoskeletons: A Review. *Sensors* **2022**, *22*, 884. [CrossRef]
10. Ko, H.; Lee, S.; Koo, D.; Lee, I.; Hyun, D. Waist-assistive exoskeleton powered by a singular actuation mechanism for prevention of back-injury. *Robot. Auton. Syst.* **2018**, *107*, 1–9. [CrossRef]
11. Li, Y.; Guan, X.; Han, X.; Tang, Z.; Meng, K.; Shi, Z.; Penzlin, B.; Yang, Y.; Ren, J.; Yang, Z.; et al. Design and preliminary validation of a lower limb exoskeleton with compact and modular actuation. *IEEE Access* **2020**, *8*, 66338–66352. [CrossRef]
12. Mori, K.; Fujimoto, Y. Implementation of Motion Intention Prediction to Highly Back-Drivable Exoskeleton. In Proceedings of the IECON 2023-49th Annual Conference Of The IEEE Industrial Electronics Society, Singapore, 16–19 October 2023; pp. 1–6.

13. Zhu, H.; Nesler, C.; Divekar, N.; Peddinti, V.; Gregg, R. Design principles for compact, backdrivable actuation in partial-assist powered knee orthoses. *IEEE/ASME Trans. Mechatron.* **2021**, *26*, 3104–3115. [CrossRef] [PubMed]
14. Mian, S.; Abouel Nasr, E.; Moiduddin, K.; Saleh, M.; Alkhalefah, H. An Insight into the Characteristics of 3D Printed Polymer Materials for Orthoses Applications: Experimental Study. *Polymers* **2024**, *16*, 403. [CrossRef] [PubMed]
15. Roveda, L.; Pesenti, M.; Rossi, M.; Rodriguez, M.; Pedrocchi, A.; Braghin, F.; Gandolla, M. User-centered back-support exoskeleton: Design and prototyping. *Procedia CIRP* **2022**, *107*, 522–527. [CrossRef]
16. Iizuka, K.; Takesue, N. Comparison of Characteristics of Internal Planetary Gear Reducer with Epitrochoid Curve using Metal and 3D Printed Parts. In Proceedings of the 2023 IEEE/SICE International Symposium On System Integration (SII), Atlanta, GA, USA, 17–20 January 2023; pp. 1–6.
17. Tunalioglu, M.; Agca, B. Wear and service life of 3-D printed polymeric gears. *Polymers* **2022**, *14*, 2064. [CrossRef]
18. Zhang, Y.; Mao, K.; Leigh, S.; Shah, A.; Chao, Z.; Ma, G. A parametric study of 3D printed polymer gears. *Int. J. Adv. Manuf. Technol.* **2020**, *107*, 4481–4492. [CrossRef]
19. Muminović, A.; Braut, S.; Božić, Ž.; Pervan, N.; Skoblar, A. Experimental failure analysis of polylactic acid gears made by additive manufacturing. *Procedia Struct. Integr.* **2023**, *46*, 125–130. [CrossRef]
20. Ciobanu, R.; Rizescu, C.; Rizescu, D.; Gramescu, B. Surface Durability of 3D-Printed Polymer Gears. *Appl. Sci.* **2024**, *14*, 2531. [CrossRef]
21. Buj-Corral, I.; Zayas-Figueras, E. Comparative study about dimensional accuracy and form errors of FFF printed spur gears using PLA and Nylon. *Polym. Test.* **2023**, *117*, 107862. [CrossRef]
22. Jiang, S.; Hu, K.; Zhan, Y.; Zhao, C.; Li, X. Theoretical and experimental investigation on the 3D surface roughness of material extrusion additive manufacturing products. *Polymers* **2022**, *14*, 293. [CrossRef]
23. Barsomian, C.; Eswaran, N.; Pesenti, M.; Gandolla, M.; Braghin, F.; Carpanzano, E.; Roveda, L. Dynamic characterization and control of a back-support exoskeleton 3D-printed cycloidal actuator. *CIRP Ann.* **2024**, *73*, 29–32. [CrossRef]
24. Sanchez, A.; Rossos, T.; Mihailidis, A.; Laschowski, B. Preliminary Development of a Robotic Hip-Knee Exoskeleton With 3D-Printed Backdrivable Actuators. In Proceedings of the International Design Engineering Technical Conferences And Computers And Information In Engineering Conference, Washington, DC, USA, 25–28 August 2024; Volume 87363, p. V008T08A072.
25. Liu, Y.; Zhang, L.; Wang, R.; Smith, C.; Gutierrez-Farewik, E. Weight distribution of a knee exoskeleton influences muscle activities during movements. *IEEE Access* **2021**, *9*, 91614–91624. [CrossRef]
26. Urs, K.; Adu, C.; Rouse, E.; Moore, T. Design and characterization of 3d printed, open-source actuators for legged locomotion. In Proceedings of the 2022 IEEE/RSJ International Conference On Intelligent Robots And Systems (IROS), Kyoto, Japan, 23–27 October 2022; pp. 1957–1964.
27. Yoshida, T.; Endo, G.; Okubo, A.; Nabae, H. Experimental Evaluation of a Quasi-direct-drive Actuator with a 3D-printed Planetary Gear Reducer. In Proceedings of the 2023 IEEE/SICE International Symposium On System Integration (SII), Atlanta, GA, USA, 17–20 January 2023; pp. 1–6.
28. Roozing, W.; Roozing, G. 3D-printable low-reduction cycloidal gearing for robotics. In Proceedings of the 2022 IEEE/RSJ International Conference On Intelligent Robots And Systems (IROS), Kyoto, Japan, 23–27 October 2022; pp. 1929–1935.
29. Roozing, W.; Roozing, G. Experimental comparison of pinwheel and non-pinwheel designs of 3D-printed cycloidal gearing for robotics. In Proceedings of the 2024 IEEE International Conference On Robotics And Automation (ICRA), Yokohama, Japan, 13–17 May 2024; pp. 7091–7098.
30. Chen, B.; Fang, T.; Li, C.; Wang, S. Gear geometry of cycloid drives. *SCience China Ser. Technol. Sci.* **2008**, *51*, 598–610. [CrossRef]
31. Blagojevic, M.; Marjanovic, N.; Djordjevic, Z.; Stojanovic, B.; Disic, A. A new design of a two-stage cycloidal speed reducer. *J. Mech. Des.* **2011**, *133*, 085001-1. [CrossRef]
32. Lin, T.; Schabacker, M.; Ho, Y.; Kuo, T.; Tsay, D. Geometric Design and Dynamic Analysis of a Compact Cam Reducer. *Machines* **2022**, *10*, 955. [CrossRef]
33. Lin, W.; Shih, Y.; Lee, J. Design of a two-stage cycloidal gear reducer with tooth modifications. *Mech. Mach. Theory* **2014**, *79*, 184–197. [CrossRef]
34. Kapelevich, A.; AKGears, L. High gear ratio epicyclic drives analysis. *Ratio* **2013**, *3*, 62–67.
35. Matsuki, H.; Nagano, K.; Fujimoto, Y. Bilateral drive gear—A highly backdrivable reduction gearbox for robotic actuators. *IEEE/Asme Trans. Mechatron.* **2019**, *24*, 2661–2673. [CrossRef]
36. Huang, X.; Rui, Y.; Wang, C.; Huang, H.; Zhang, Z.; Fan, C.; Yang, Y. Gravity Compensation Based Control for Lower-Limb Load-Bearing Exoskeleton. In Proceedings of the 2021 6th International Conference On Control, Robotics And Cybernetics (CRC), Shanghai, China, 9–11 October 2021; pp. 230–234.
37. Satake, H.; Takesue, N. Comparison of Characteristics of Cycloidal Gear Reducer Using Metal, Plastic and 3D Printed Parts. In Proceedings of the 2024 IEEE/SICE International Symposium On System Integration (SII), Ha Long, Vietnam, 8–11 January 2024; pp. 1531–1536.

Disclaimer/Publisher's Note: The statements, opinions and data contained in all publications are solely those of the individual author(s) and contributor(s) and not of MDPI and/or the editor(s). MDPI and/or the editor(s) disclaim responsibility for any injury to people or property resulting from any ideas, methods, instructions or products referred to in the content.